

Novel iGSE-C Loss Modeling of X7R Ceramic Capacitors

David Menzi [✉], *Student Member, IEEE*, Dominik Bortis [✉], *Member, IEEE*,
Grayson Zulauf [✉], *Student Member, IEEE*, Morris Heller [✉], *Student Member, IEEE*,
and Johann W. Kolar [✉], *Fellow, IEEE*

Abstract—Due to the large relative permittivity of Class II dielectrics, ceramic capacitors (CCs) from these materials promise significant volume and weight reductions in inverter and rectifier sine-wave filters, and are especially attractive in mobile applications that demand ultrahigh power density. While previous literature found large low-frequency losses in these components, no extensible loss model was proposed to accurately characterize these ferroelectric losses. In this article, we take advantage of prior art on ferromagnetic components in power electronics to propose a Steinmetz parameter-based loss modeling approach for X7R CCs, named the Improved Generalized Steinmetz Equation for CCs, or iGSE-C. This model is verified using the Sawyer–Tower circuit to measure losses in a commercially available X7R capacitor across excitation magnitude, dc bias, temperature, excitation frequency, and harmonic injection. Losses are shown to scale according to a power law with charge, with the resulting Steinmetz coefficients valid across dc bias and slightly varying as the temperature is increased. The iGSE-C accurately predicts losses for typical nonsinusoidal phase voltage waveforms with an error under 8%. Finally, the loss modeling technique is demonstrated for the sine-wave output filter of a bridge-leg arrangement with both low- and high-frequency excitations, with total capacitor losses predicted within 12% accuracy.

Index Terms—AC–DC power converters, ceramic capacitors (CCs), dc–ac power converters, inverters, improved generalized Steinmetz equation (iGSE), iGSE for CCs (iGSE-C), large-signal excitation, power capacitors, rectifiers, Steinmetz loss modeling.

I. INTRODUCTION

IN THE push toward ultracompact power converters for emerging applications, including electric vehicles and more-electric aircraft, electromagnetic interference (EMI) filter volume and weight represent a key bottleneck to ever-higher volumetric and gravimetric power density. In switched-mode converters, these filters are unavoidable to protect the mains from high-frequency conducted emissions and to comply with the relevant harmonic standards, and a path toward both miniaturization and weight reduction is sought.

Manuscript received February 4, 2020; revised April 2, 2020; accepted May 14, 2020. Date of publication May 19, 2020; date of current version July 31, 2020. Recommended for publication by Associate Editor M. Chen. (*Corresponding author: David Menzi.*)

The authors are with the Power Electronic Systems Laboratory, ETH Zurich, 8092 Zurich, Switzerland (e-mail: menzi@lem.ee.ethz.ch; bortis@lem.ee.ethz.ch; zulauf@lem.ee.ethz.ch; heller@lem.ee.ethz.ch; kolar@lem.ee.ethz.ch).

Color versions of one or more of the figures in this article are available online at <https://ieeexplore.ieee.org>.

Digital Object Identifier 10.1109/TPEL.2020.2996010

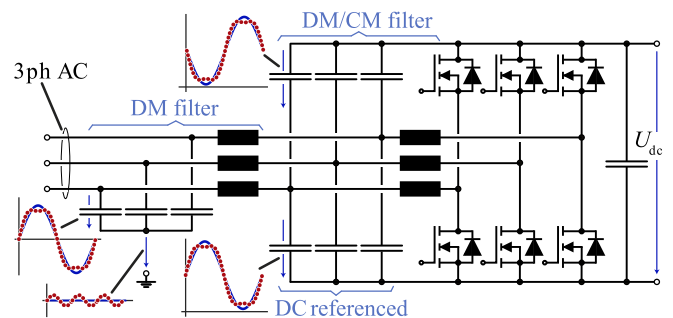


Fig. 1. Illustration of a common sine-wave filter structure for a three-phase inverter or PFC rectifier: open-star-point Differential Mode (DM) filter and combined DM/Common Mode (CM) dc-link referenced filter. The resulting low-frequency voltage waveforms across the filter capacitors for standard sinusoidal PWM operation with constant dc offset (solid line) and with additional 1/6 third harmonic injection [3] (dotted line) for maximum utilization of the linear modulation range are shown.

TABLE I
COMPARISON OF A FILM AND A CC

Dielectric	V_n	C_n	Volume	Price
Film (PP)	1 kV	470 nF	9.87 cm ³	1.94 \$
Ceramic (X7R)	1 kV	470 nF	0.13 cm ³	6.69 \$

For the sine-wave filters of, e.g., three-phase rectifiers or motor drive systems with low high-frequency stresses (to reduce bearing currents and/or increase feasible cable lengths), a variety of filtering techniques—both common mode (CM) and differential mode (DM)—are employed to filter switching harmonics while passing the fundamental frequency, as shown in Fig. 1. Due to their low cost and high quality factor [1], film capacitors are predominantly used in these applications, comprising approximately 50% of the overall filter volume [2].

To reduce the filter volume and weight in applications highly sensitive to power density, ceramic capacitors (CCs) are an attractive replacement for film capacitors [4]. For a 1 kV, 470 nF capacitor, the volume can be reduced by over 75 \times by moving from an off-the-shelf film capacitor (metallized polypropylene, KEMET PHE844RD6470MR30L2) to an off-the-shelf CC (X7R, Knowles Syfer 2220Y1K00474KETWS2), as shown in Table I. With this one-for-one replacement, the capacitor contribution to the filter volume becomes negligible, allowing the inductor size to be increased (reducing losses and improving

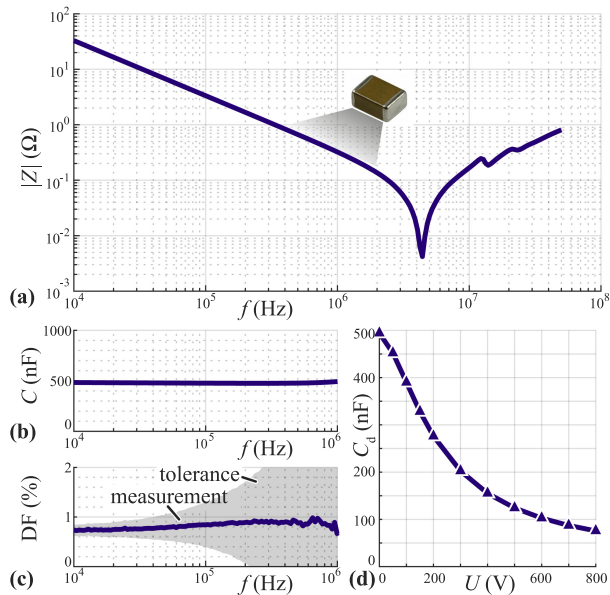


Fig. 2. Small-signal measurements of (a) impedance, (b) capacitance, and (c) DF of the 1kV, 470nF, X7R CC under test (Knowles Syfer 2220Y1K00474KETWS2) at room temperature (25° C) and with 0.5 V_{rms} ac excitation. Self-resonance occurs at 4.4 MHz. The small-signal capacitance dependence on voltage is shown in (d), where an ac excitation of 5 V_{rms} with 100 Hz was applied on top of the reported dc bias voltage U .

efficiency) and/or a reduction in overall converter size and weight. As such, CCs are the preferred capacitor technology for ultracompact converters, including those built for the Google Little Box Challenge [5], [6] and/or for any application, where the benefits of compactness outweigh the cost increase of the ceramic replacement (costs given in Table I).

In particular, X7R CCs have extremely high capacitance and energy density [1], originating from the large relative permittivity of ferroelectric Class II dielectrics [7]. X7R capacitors have excellent properties in the high-frequency range for filtering switching harmonics, with a constant capacitance value over a wide frequency range, low effective series resistance (ESR), and a compact geometry that enables a low-inductance realization with a high self-resonant frequency [see the small-signal impedance measurements of the 2220Y1K00474KETWS2 capacitor in Fig. 2(a)–(c)]. With increasing voltage bias, however, X7R CCs exhibit (similar to magnetic components) dielectric saturation [8] and a decrease in capacitance, as measured in Fig. 2(d), well-known in the literature (e.g., [9]), and reported in capacitor datasheets.

In the context of line-frequency filtering, the effective capacitance is then highly dependent on the low-frequency voltage waveforms and, therefore, on the filter configuration itself. To highlight these voltage waveforms, Fig. 1 shows both a combined DM/CM dc-link referenced LC -filter, which was proposed in [10] specifically to reduce the capacitance variation in a line cycle, and a pure DM filter structure. In motor drive applications, alternative modulation schemes employed to expand the modulation range and/or to decrease semiconductor losses [11] introduce additional harmonics (e.g., third harmonic injection [3] or discontinuous pulsewidth modulation (PWM) [12]),

which further impacts the voltages applied to the filter capacitors. Fig. 1 accordingly includes the resulting low-frequency capacitor voltages for both standard sinusoidal modulation and additional third harmonic injection. Finally, the filter capacitors connected to the dc-link rails in Fig. 1 also face the triangular switching-frequency currents of the power inductors, causing a voltage variation and losses on a switching frequency level. Furthermore, high-frequency stresses are possible in alternative topologies such as the three-phase Y-inverter [13], where the filter capacitors are subject to both low-frequency voltage waveforms with a dc offset and rectangular switching-frequency currents.

Recent work has found an elevated dissipation factor (DF) in CCs operating at low frequencies that is highly dependent on both dc bias and the large-signal excitation frequency and waveshape [14], [15]. These unexpectedly high losses—as high as 10 W cm^{-3} at 120 Hz [14]—cannot be predicted from the small-signal measurement data provided by manufacturers (in the datasheet or with online tools), and indeed Mosley *et al.* [16] described that small-signal measurements are fundamentally insufficient to characterize a ferroelectric capacitor. Within the context of elevated large-signal excitation losses, the compactness of CCs becomes a double-edged sword: although the loss contribution of CCs in a converter system may still be relatively small, substantial capacitor heating can result, eventually limiting, for example, the maximum fundamental frequency (and hence speed) for a motor drive system. In light of these unmodeled and substantial large-signal losses, we desire a method—extensible across voltage waveshape—to measure, characterize, and predict these losses in CCs.

For magnetic components, which also exhibit loss mechanisms that must be characterized under large-signal conditions, Steinmetz parameters [17] are commonly provided to allow engineers to calculate core losses under a particular operating condition. Whereas Neumayr *et al.* [14] and Coday *et al.* [15] only provided loss lookup tables for the reported CCs under a sine-wave excitation at a few frequencies and a multitude of dc bias points, leaving extensibility across dc voltage, ac waveshape, frequency, and part number unanswered. The current state of the art, then, requires additional measurements to design CC filters with losses that can be predicted *a priori* (excluding the coincidence when the filter capacitor, frequency, and selected part all exactly align with a reported measurement point).

Given these shortcomings and the attractiveness of CCs for converters with high power density, there is a clear need for a loss model for ferroelectric capacitors in power electronics. In this article, we propose a Steinmetz-based loss modeling approach for CCs under large-signal excitation, called the improved generalized Steinmetz equation for ceramic capacitors (iGSE-C), in Section II, which is verified with the measurement technique of Section III on a commercially available ferroelectric capacitor in Section IV. This particular capacitor, or the device under test (DUT), is the 1kV, 470nF X7R CC of Table II, which was employed in a hardware prototype for an ultracompact industrial motor drive with large observed low-frequency excitation losses. Low-frequency losses are characterized across excitation magnitude, dc bias, temperature, and third harmonic content.

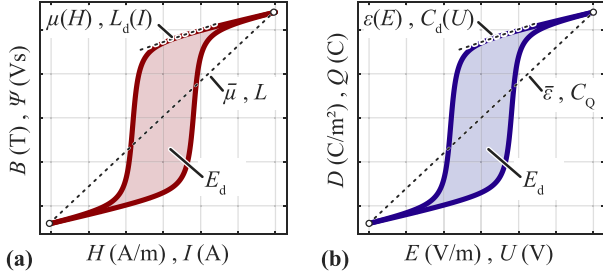


Fig. 3. Illustration of a (a) ferromagnetic and (b) ferroelectric hysteresis loop, with instantaneous (L_d, C_d) inductances and capacitances highlighted separately from average large-signal values (L, C_Q).

Next, high-frequency losses are added for a complete picture of X7R CC losses in switched-mode power converters, which is validated in Section V with straightforward and extensible design guidelines for loss prediction *in situ* based on the iGSE-C. Section VI summarizes the key findings and the proposed iGSE-C model, and Appendix A surveys alternative calorimetric-based loss measurement techniques.

II. MODELING APPROACH

For adoption and adaptability, the ferroelectric capacitor loss modeling approach must be extensible across voltage waveform, excitation magnitude, and dc bias. A Steinmetz-based capacitor loss model is developed analogously to the well-known large-signal approach for ferromagnetic components, and we first review the conventional [17] and improved generalized steinmetz equation (iGSE) [18] for inductors to ground the proposed model.

A ferromagnetic hysteresis loop is shown in Fig. 3(a), where the magnetic field strength H (or current I) and flux density B (or flux linkage, Ψ , given by the time integral of the excitation voltage U) are linked by the permeability $\mu(H)$ (or differential inductance $L_d(I)$) as

$$L_d(I) = \frac{U}{dI/dt} = \frac{d\Psi}{dI}, \quad \mu(H) = \frac{dB}{dH}. \quad (1)$$

For a given hysteresis curve, both the average permeability $\bar{\mu}$ (or large-signal inductance L) and instantaneous permeability $\mu(H)$ can be calculated, and these are shown on Fig. 3(a) as the appropriate slopes. The enclosed area E_d represents the energy dissipated in a single charge–discharge cycle, where hysteresis (caused by irreversible magnetization), eddy current, and residual losses are the main underlying loss mechanisms [19].

The time-averaged losses P of magnetic materials under a sinusoidal flux excitation depend on both frequency f and the peak magnetic flux density, B_{pk} , and empirically follows the power law given by the familiar Steinmetz equation (SE) [17]

$$P = k \cdot f^\alpha \cdot B_{pk}^\beta \quad (2)$$

where k , α , and β are material-specific constants characterized under large-signal excitation (note that f^α was not in the original equation, but was added later and is now standard [18]).

For a nonsinusoidal excitation—the condition in most power converters—a number of loss-modeling methods have been proposed. The iGSE [18] is the most established method, and one with parameters directly extractable from the given Steinmetz parameters. The losses are assumed to depend both on the peak-to-peak flux density ΔB and the flux density change rate dB/dt within a period T as

$$P = k_i \cdot \Delta B^{\beta-\alpha} \cdot \frac{1}{T} \int_0^T \left| \frac{dB}{dt} \right|^\alpha dt \quad (3)$$

with the coefficient k_i derived from the SE parameters as

$$k_i = \frac{k}{(2\pi)^{\alpha-1} \int_0^{2\pi} |\cos \theta|^{\alpha} 2^{\beta-\alpha} d\theta}. \quad (4)$$

If multiple minor hysteresis loops occur within a single period T , (3) is summed for each loop j separately to find average core losses as

$$P_{avg} = \sum_j P_j \frac{T_j}{T}. \quad (5)$$

With the SE and iGSE well-established for magnetic materials, we seek to develop an analogous loss modeling method for ferroelectric capacitors, including the ceramic components highlighted here. Fig. 3(b) shows a ferroelectric hysteresis loop, where the electric field strength E (or voltage U) and displacement field D (or charge Q) are linked by the permittivity $\varepsilon(E)$ (or differential capacitance $C_d(U)$) as

$$C_d(U) = \frac{I}{dU/dt} = \frac{dQ}{dU}, \quad \varepsilon(E) = \frac{dD}{dE}. \quad (6)$$

For a given hysteresis curve, both the average permittivity $\bar{\varepsilon}$ (or charge-equivalent capacitance C_Q) [20] and instantaneous permittivity $\varepsilon(E)$ can be calculated, and these are shown in Fig. 3(b) as the appropriate slopes. Again, the area enclosed by the loop E_d represents the energy dissipated in a single charge–discharge cycle. In [21], a summary of capacitor losses mechanisms is provided, where ferroelectric Class II CC hysteresis losses result (similar to the hysteresis losses in magnetics) due to irreversible polarization processes [22], [23].

Ben-Yaakov [24] proposed a Steinmetz power law to model ferroelectric capacitor losses under small-signal excitation with a fit on the peak sinusoidal voltage, \hat{U} . The same voltage-based Steinmetz template was used for losses in semiconductor output capacitance in [25] and [26], where multiple sets of Steinmetz parameters were required to accurately describe the losses over the excitation voltage range. With the curve of Fig. 3(b), however, we see that a power law fit on excitation voltage (or field strength E) cannot hold in a ferroelectric capacitor due to the charge saturation with increasing voltage magnitude. Steinmetz [27] also worked on dielectric hysteresis and expected, based on theoretical considerations only, the losses to scale with $P = kfD_{pk}^2$ for a peak charge density excitation D_{pk} . In contrast to magnetic materials, the field quantity D of commercial CCs cannot be easily calculated, as the internal structure, and, therefore, the effective amount of dielectric material and electrode area per device volume, is not known (cf., Fig. 4). However, the charge

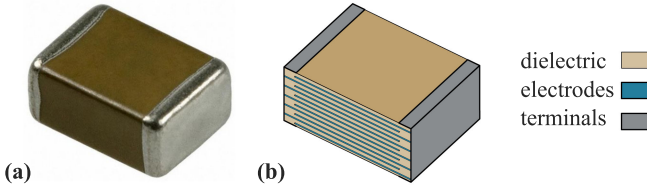


Fig. 4. (a) Picture of the 1kV, 470nF, X7R CC under test (Knowles Syfer 2220Y1K00474KETWS2) and (b) illustration of the internal structure of a Ceramic Capacitor (CC) consisting of several electrode and dielectric layers. The resulting capacitance value depends on the employed dielectric and the number, arrangement, and thickness of the electrodes[9]. These parameters are not known for commercial devices.

Q can be measured without in-depth knowledge of the exact CC realization.

Therefore, and in analogy with the ferromagnetic SE of (2), we propose to describe the losses in ferroelectric capacitors with a *peak charge based* (Q_{pk}) SE as

$$P = k \cdot f^\alpha \cdot Q_{pk}^\beta \quad (7)$$

where k , α , and β are to be fitted under large-signal excitation. We note that SE parameters found for one CC cannot directly be employed for another product (even when the same dielectric is employed), as the charge density D is not known. However, in future datasheets, device manufacturers could provide the SE parameters of the employed dielectric and the dielectric volume density for each product to support loss calculations.

For nonsinusoidal excitations, an iGSE approach could again be applied, where for a peak-to-peak charge ΔQ , the losses can be described

$$P = k_i \cdot \Delta Q^{\beta-\alpha} \cdot \frac{1}{T} \int_0^T \left| \frac{dQ}{dt} \right|^\alpha dt \quad (8)$$

and k_i is again given by the SE parameters and (4), where (8) collapses to (7) in the case of a sinusoidal excitation. This proposed loss model is named the improved generalized Steinmetz equation for ceramic capacitors, or the iGSE-C.

III. MEASUREMENT METHOD AND SETUP

With a modeling approach proposed, we turn to characterizing the losses in the selected X7R CC of Table II. First, a measurement method must be selected that can evaluate the known loss dependencies outlined in Section I of

- 1) large-signal excitation (sinusoidal and nonsinusoidal);
- 2) dc bias;
- 3) frequency;
- 4) high-frequency currents; and
- 5) temperature.

Ideally, this measurement method produces rapid measurements that can be applied to transient conditions, can measure losses at constant temperature, is applicable across a wide frequency range, and is valid with nonsinusoidal waveforms. We briefly survey potential electric and calorimetric methods.

A. Potential Measurement Techniques

1) *Voltage–Current Electric Measurement*: A voltage–current electric measurement that measures instantaneous power

with a voltage and current probe is one candidate for loss characterization. This method fulfills the need for fast, quasi-pulse measurements in a time period that avoids a substantial increase of the DUT temperature, and Neumayr *et al.* [14] used a Yokogawa WT3000 power analyzer to measure the losses in two ferroelectric capacitors under 120 Hz large-signal excitation. Coday *et al.* [15] used a similar measurement approach to validate a calorimetric measurement and calculate volumetric energy storage at low frequencies.

This direct measurement method introduces a number of challenges, however. For a high-quality factor CC avoiding a phase error between the voltage and current probes is paramount and, unfortunately, difficult to maintain across excitation frequency and when nonsinusoidal waveforms are applied. To overcome this problematic calibration step, currents could be measured with a precision shunt and a voltage probe to simplify phase matching. With the current of a capacitor scaling linearly with frequency (for a constant voltage), however, a large number of shunts would be required to achieve a good signal-to-noise ratio for a frequency range of several orders of magnitude.

2) *Sawyer–Tower (ST) Electric Measurement*: The ST method was introduced in 1930 [28] to evaluate Rochelle salt as a dielectric, and operates by adding a well-characterized, low-loss reference capacitor in series with the DUT to calculate the charge in the DUT. This method has been employed in various power electronics applications, including characterizing capacitors for microprocessor applications [29] and to measure soft-switching losses (up to the MHz frequency range) in silicon superjunction MOSFETs [25], SiC MOSFETs [30], and GaN-on-Si HEMTs [26]. For semiconductor-specific measurements, the ST circuit was improved and simplified in [31].

The ST measurements are conducted with passive voltage probes, and with the voltage ratio between the DUT and the reference capacitor constant over frequency, a single ST setup can be used to cover the whole frequency range of interest.

3) *Calorimetric Measurements*: Calorimetric measurement techniques achieve excellent accuracy independent of frequency and the ratio of reactive to active power, and have been used to characterize capacitor losses [15], [32], [33]. Appendix A surveys three calorimetric measurement types [(a) steady-state, (b) indirect transient, and (c) direct transient], finding that none are attractive for the application, because of the temperature dependence of the losses of CCs for (a), the slow speed of calorimetric measurements for (b), and the lack of a known loss calibration point in a capacitor in case of (c).

Therefore, with the ease of calibration, extensibility across waveforms, and transient measurement capability, the ST method is the preferred candidate for this measurement suite, and the circuit operation is covered in detail below.

B. ST Measurement

The ST circuit is shown in Fig. 5(a), with both the voltage across the linear reference capacitor C_{ref} (u_{ref}) and the excitation voltage u_{ac} measured. Depending on the position of the mechanical switch, either the lossy and nonlinear DUT or the calibration capacitor C_{cal} is measured, where C_{cal} is ideally linear and

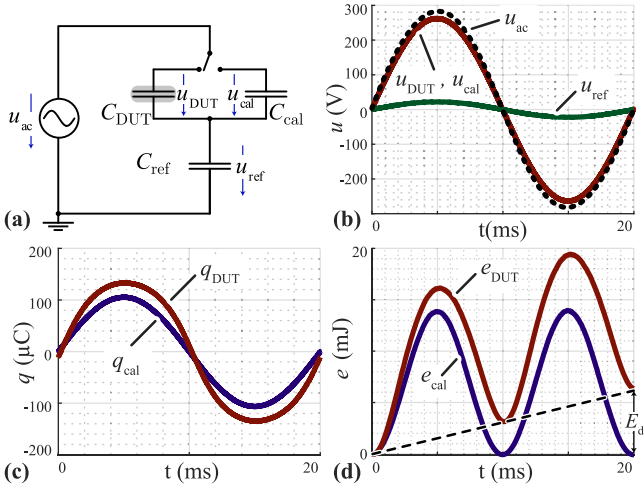


Fig. 5. (a) Schematic circuit of the employed ST measurement setup (either the Device Under Test (DUT) or a calibration capacitor is connected in series to the reference capacitor) for ac voltage excitation. Resulting time-domain waveforms for the Sawyer-Tower (ST) measurement: (b) voltage, (c) calculated charge, and (d) calculated stored energy. For the lossless calibration capacitor, the stored energy e_{cal} is fully recovered within an ac period, giving identical initial and final energy. For the lossy DUT, however, some portion of the stored energy is dissipated, yielding a final e_{DUT} larger than the initial e_{DUT} (the distance of which is represented by E_d).

lossless and serves to calibrate the ST setup. The component selection for the realization of C_{ref} and C_{cal} is discussed in further detail at the end of this section, where nonferroelectric COG capacitors with a 20x to 30x lower DF than the class II ferroelectric CCs of interest are employed (cf., Table II).

The measured voltage waveforms are shown for operation with both C_{cal} and C_{DUT} in Fig. 5(b), and the component values according to Table II. With the charge q [c.f., Fig. 5(c)] in series capacitors equal, we can write (note that the following loss equation is derived for the DUT, but the same equations and procedure apply for the calibration capacitor C_{cal})

$$u_{DUT}(t) = u_{ac}(t) - u_{ref}(t) \quad (9)$$

$$q_{DUT}(t) = q_{ref}(t) = u_{ref}(t) \cdot C_{ref}. \quad (10)$$

With C_{ref} selected as much higher capacitance than C_{DUT} or C_{cal} , only a small fraction of the applied voltage u_{ac} appears across it [cf., Fig. 5(b)].

Integrating the instantaneous power, the energy stored in the nonlinear DUT [cf., Fig. 5(d)] can be calculated using the calculated charge q_{DUT} (10) as

$$\begin{aligned} e_{DUT}(t) &= \int_0^t u_{DUT}(\tau) \cdot i_{DUT}(\tau) d\tau \\ &= \int_0^t u_{DUT}(\tau) \cdot \frac{dq_{DUT}}{d\tau} d\tau = \int_{q_{DUT}(0)}^{q_{DUT}(t)} u_{DUT} dq_{DUT}. \end{aligned} \quad (11)$$

For a signal periodic with T (i.e., $u_{DUT}(0) = u_{DUT}(T)$ and $q_{DUT}(0) = q_{DUT}(T)$) and starting with the global charge minima $q_{DUT}(0) = q_{min}$, the dissipated energy E_d [i.e., the area enclosed by the U - Q hysteresis loop in Fig. 3(b)] of one cycle

can be calculated, which yields the active power

$$\begin{aligned} P &= \frac{E_d}{T} \\ &= \frac{1}{T} \left(\underbrace{\int_{q_{DUT}(0)}^{q_{DUT}(T/2)} u_{DUT} dq_{DUT}}_{\text{charge}} + \underbrace{\int_{q_{DUT}(T/2)}^{q_{DUT}(T)} u_{DUT} dq_{DUT}}_{\text{discharge}} \right). \end{aligned} \quad (12)$$

E_d is highlighted in Fig. 5(d) for the DUT, which stands in contrast to the calibration capacitor (in the same figure) where all of the stored energy is recovered. The DF is defined by the ratio of dissipated E_d and stored E_{stored} energy

$$DF = \frac{E_d}{2\pi \cdot E_{stored}} \quad (13)$$

and is a good measure for the loss-rate of nonlinear CCs. For a linear capacitor (or a nonlinear capacitor with small-signal excitation), the DF is identical to the loss tangent $\tan(\delta)$ (i.e., the ratio of active and reactive power).

When C_{cal} is measured, two linear capacitors are excited by the sinusoidal voltage u_{ac} , resulting in the sinusoidal charge waveform q_{cal} of Fig. 5(c). The nonlinearity of C_{DUT} , however, causes the charge waveform q_{DUT} not to be purely sinusoidal, shown for contrast in Fig. 5(c).

The selection of C_{ref} is critical for the accuracy of the ST measurements, and we highlight the key characteristics here. First, C_{ref} takes a certain fraction of the applied ac voltage, which should be kept relatively small, such that the DUT sees the majority of the excitation voltage U_{ac} . This can be achieved with $C_{ref} \gg C_{DUT}$, where a reasonable choice might be $C_{ref} \approx 10 \cdot C_{DUT}$. Second, if the DUT and the reference capacitor show the same loss tangent, the two measured voltages (u_{ac} and u_{ref}) will be in phase, resulting in no measured U - Q hysteresis and zero measured losses. The reference capacitor, therefore, must have substantially lower $\tan \delta$ than the DUT. Finally, the ST is fundamentally reliant on the linearity of C_{ref} to calculate the charge from voltage [see (10)], and the reference capacitors should be highly linear, i.e., a ferroelectric Class II capacitor should not be used for C_{ref} .

In light of these requirements, C_{ref} and the calibration capacitors C_{cal} are realized with low-loss, Class I COG capacitors with extremely stable dielectrics. The key properties are summarized in Table II, with the DF of C_{ref} and C_{cal} at least an order of magnitude below the DUT [which was directly measured under small-signal conditions in Fig. 2(c)]. For the COG reference and calibration capacitors, the small-signal DF accurately approximates the large-signal DF, and the impact of the small-but-nonzero DF of C_{ref} is neglected in the following loss measurements.

With this simple and extensible technique, losses in ferroelectric capacitors can be characterized across voltage, temperature, waveform shape, dc bias, and frequency, and we move to validate the proposed loss model of Section II with measurements on the selected DUT.

TABLE II
EMPLOYED COMPONENTS

Component	Dielectric	Manufacturer	Part Number	V_n	C_n	N(parallel)	C_{tot}	DF
C_{cal}	COG	TDK	CAA572C0G2J204J640LH	650 V	200 nF	2	400 nF	< 0.02 %
C_{ref}	COG	TDK	C5750C0G2A154J230KE	100 V	150 nF	32	4.8 μ F	< 0.03 %
C_{DUT}	X7R	Knowles Syfer	2220Y1K00474KETWS2	1 kV	470 nF	1	470 nF	> 0.71 %

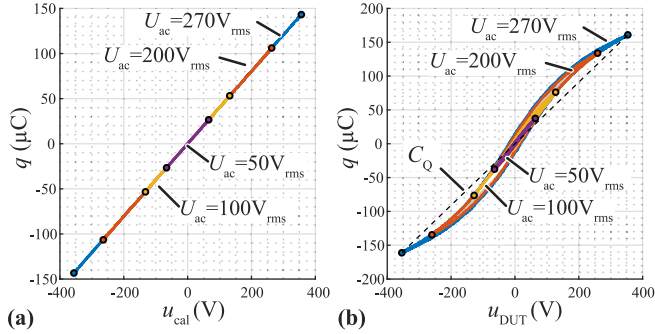


Fig. 6. $U - Q$ hysteresis recorded at 50 Hz for a range of excitation voltages for (a) the calibration capacitor, which shows no hysteresis and has a constant $C_Q = C_d$ at all voltages, and (b) the DUT, which exhibits increasing hysteresis and losses with increasing excitation voltage. C_Q highlighted for $U_{ac} = 270$ V_{rms}. Measured $U - Q$ curves are identical at 50 Hz and 100 Hz.

IV. EXPERIMENTAL RESULTS

A sinusoidal ac excitation is applied to the circuit of Fig. 5(a) with an ac power source ($U_{ac,max} = 270$ V_{rms}), with the initial calibration measurements shown at 50 Hz for a range of excitation voltages in Fig. 6.

With the calibration COG capacitor [see Fig. 6(a)], the capacitance is linear for all magnitudes, resulting in a constant C_Q across voltage and $C_Q = C_d$. There is no measurable hysteresis between the charging and discharging curves at a given voltage, resulting in negligible losses that are verified with no heating of C_{cal} during the test procedure. This “zero-loss” reading also validates a proper deskew of the voltage probes.

For the same excitation voltages at 50 Hz, Fig. 6(b) shows the measured ferroelectric $U_{DUT} - Q$ hysteresis curves for the X7R DUT capacitor. At 50 V_{rms}, the capacitor is approximately linear ($C_Q \approx C_d$), but clearly starts saturating for higher excitation amplitude. C_Q changes across applied voltage, and C_d deviates from C_Q at different voltages along the $U_{DUT} - Q$ curve. With an increasing voltage, further, the hysteresis area between the charging and discharging curves expands (especially near the zero-crossing, as we return to later), indicating an increase in losses with excitation voltage.

Even at the line frequency of 50 Hz, these hysteretic losses total as high as 0.5 W per DUT capacitor, and the large-signal DF is nearly an order-of-magnitude higher than the small-signal DF measured in Fig. 2(c). These significant losses, validated by [14] and [15], justify a deeper investigation of the key loss drivers, and we evaluate the impact of frequency and excitation magnitude based on the proposed SE (see Section IV-A), harmonic injection based on the proposed iGSE-C (see Section IV-B), dc bias (see Section IV-C), temperature (see Section IV-D), and, finally, the impact of the high-frequency excitations necessarily

imposed by the switching frequency current ripple of the inductors connected to the half-bridge switched nodes in Fig. 1 (see Section IV-E).

A. Impact of AC Excitation Magnitude and Frequency

The impact of low-frequency excitation voltage and frequency are evaluated from, respectively, 50–250 V_{rms} and 50–250 Hz. These measurements are recorded at room temperature (25° C) with a measurement time of 1 s to avoid self-heating of C_{DUT} and to isolate any impact of temperature on the losses. The impact of temperature is investigated later in Section IV-D, where we find that self-heating of up to 10° C changes the losses by no more than $\approx 5\%$ for the operating points considered here.

The measured losses are shown in Fig. 7. First, we note the measured DF exceeds 7.0% under certain operating conditions, far above the 0.7% predicted by the small-signal characterization of Fig. 2(c) and resulting in losses as large as 2 W. Fig. 7(a.i)–(c.i) highlights the impact across frequency, and we find a linear scaling of losses with f , supporting the finding of $\alpha = 1$ from [24] for the SE of (7). C_Q and DF do not vary across this frequency range (with the slight measured deviations attributed to measurement error and heating of the DUT). This linear loss-frequency relationship (and the identical $U - Q$ hysteresis curves across frequency) are supported by the stable capacitance value of the DUT across frequency, as observed under both small-signal [see Fig. 2(a)–(b)] and large-signal [see Fig. 7(b.i)] conditions. Therefore, when increasing the frequency for a given excitation amplitude, the same ferroelectric hysteresis curve (cf., Fig. 6) is traversed more often, dissipating a constant amount of energy per cycle and accordingly resulting in a linearly increasing power.

Across varying excitation voltage [highlighted in Fig. 7(a.ii)–(c.ii)], however, we observe significant deviations from the expected behavior of the X7R DUT capacitor. At low excitation voltage, DF approaches the small-signal value (0.7%), increases up to 7.0% at 100 V_{rms}, then saturates and even slightly decreases as the magnitude is further increased [see Fig. 7(c.ii)]. This voltage-dependent trend follows the other surprising finding that C_Q increases up to 100 V_{rms} [see Fig. 7(b.ii)]—for all X7R capacitors, we expect the capacitance to steadily decrease with voltage, as shown by the calculated charge-equivalent capacitance derived from the small-signal measurements of Fig. 2(d) [dotted line in Fig. 7(b.ii)]. The peak capacitance is over 600 nF, more than 20% greater than the measured value at zero dc bias. This effect of increasing capacitance with ac magnitude is also described in [9].

The additional capacitance indicates a large-signal polarization mechanism around the voltage zero-crossing that is not captured by measurements with small ac magnitudes. While this phenomenon is investigated more in Section IV-C, we note here

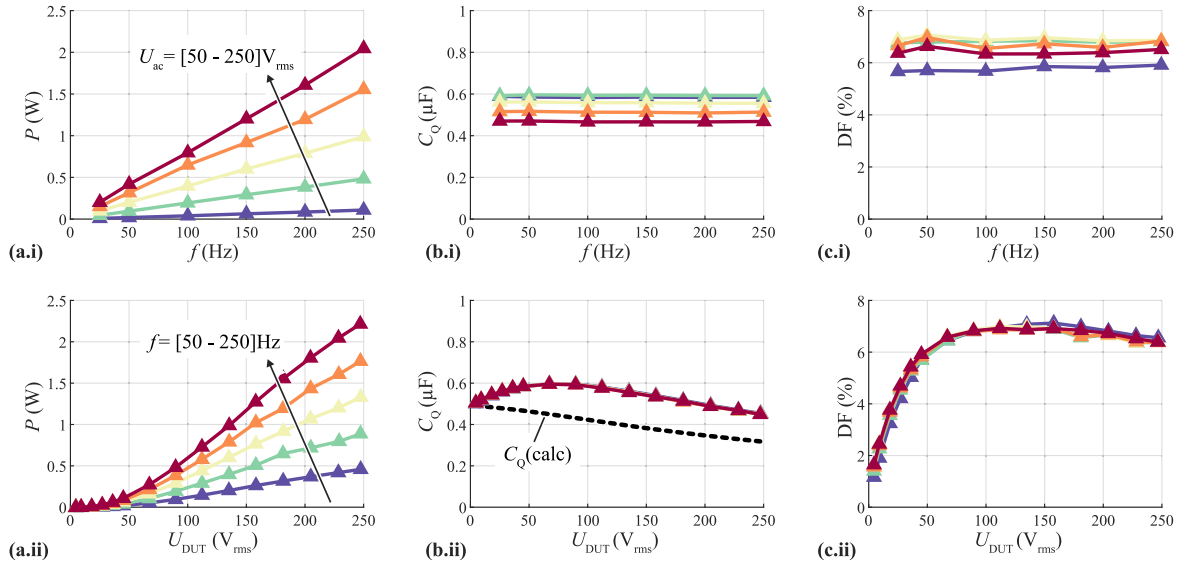


Fig. 7. Measured losses in the X7R CC DUT using the ST circuit of Fig. 5(a) across ac excitation voltage and ac excitation frequency. DF is nearly an order-of-magnitude larger than expected from the small-signal measurements [see Fig. 2(c)] and capacitance increases up to $U_{DUT} = 100 V_{rms}$. Losses linearly increase with frequency equivalent to an Steinmetz Equation (SE) parameter of $\alpha = 1$. (a) Losses P , (b) ac charge equivalent capacitance C_Q (the expected value $C_Q(\text{calc})$ derived from Fig. 2(d) is represented by the dashed line, and in (b.ii) all capacitance curves are overlapping), and (c) DF, plotted against (i) frequency and (ii) DUT voltage rms value.

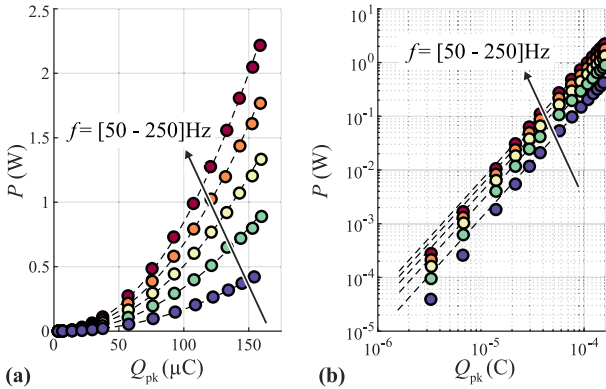


Fig. 8. Measured losses, from Fig. 7, plotted against measured charge Q_{pk} for ac frequencies from 50–250 Hz and ac voltages from 50–250 V_{rms} . Dotted lines are derived Steinmetz parameters ($k = 1.06 \cdot 10^6$, $\alpha = 1$, and $\beta = 2.12$) in (7), which show excellent agreement with the measured data. (a) Linear representation and (b) logarithmic representation.

that the extra capacitance is undesired for filtering. The fundamental reactive currents in the capacitor are $I_Q = 2\pi f C_Q U_{DUT}$, so a larger C_Q large-signal capacitance maps to increased conduction losses in the inductors and semiconductors of the converter while the capacitance available for switching-frequency filtering remains limited to the appropriate small-signal value of Fig. 2(d).

Finally, we return to the proposed charge-based SE modeling to evaluate whether the measured losses are appropriately captured by (7). In Fig. 8, the measured losses are scattered against the measured charge excitation amplitude of $Q_{pk} = C_{ref} \cdot U_{ref,pk}$ [cf., (10)] on both linear [see Fig. 8(a)] and logarithmic [see Fig. 8(b)] scales. Steinmetz parameters are fit from the measured data and plotted using (7) as dotted lines on both scales, with selected values of $k = 1.06 \cdot 10^6$, $\alpha = 1$, and $\beta =$

2.12. This fitting matches the measured data extremely well, with discrepancies only at very low excitation magnitudes where the measurement precision is low (losses in the 10 μW range), strongly supporting the proposed charge-based SE modeling approach. We note that a voltage-based power law relationship (proposed in [24] for small-signal excitation) cannot accurately capture the measured losses, as the losses have two distinct scaling regions with voltage (exponential below 50 V_{rms} , linear above 50 V_{rms}) that are clearly seen in Fig. 7(a.ii).

Our characterization of losses across voltage magnitude and frequency confirm the proposed SE fitting, finding a strong dependence of losses on peak charge (more than quadratic, with $\beta = 2.12$) and a large-signal polarization near the zero-crossing that increases both converter conduction losses and the losses in the capacitor itself. With the charge-based SE approach confirmed, we next add superimposed harmonics to evaluate the iGSE-C extension of ferroelectric capacitor losses.

B. Impact of Harmonic Injection and iGSE Modeling

Generally, the modeling approach must be valid for nonsinusoidal waveforms. For filter capacitors in motor drive inverter or three-phase power factor correction (PFC) rectifier applications, in particular, the third harmonic (and its multiples) of the fundamental frequency is often used to extend the modulation range of the PWM scheme [11]. In the proposal of the iGSE loss modeling approach for magnetic materials [18], the method was verified by superimposing a third harmonic component of varying magnitude upon the fundamental frequency excitation. Analogously, the ferroelectric iGSE-C proposed here in (8) is tested with the DUT under third harmonic injection.

1) *Methodology*: The DUT is excited with a single phase of a pre-existing buck-type three-phase inverter that complies with

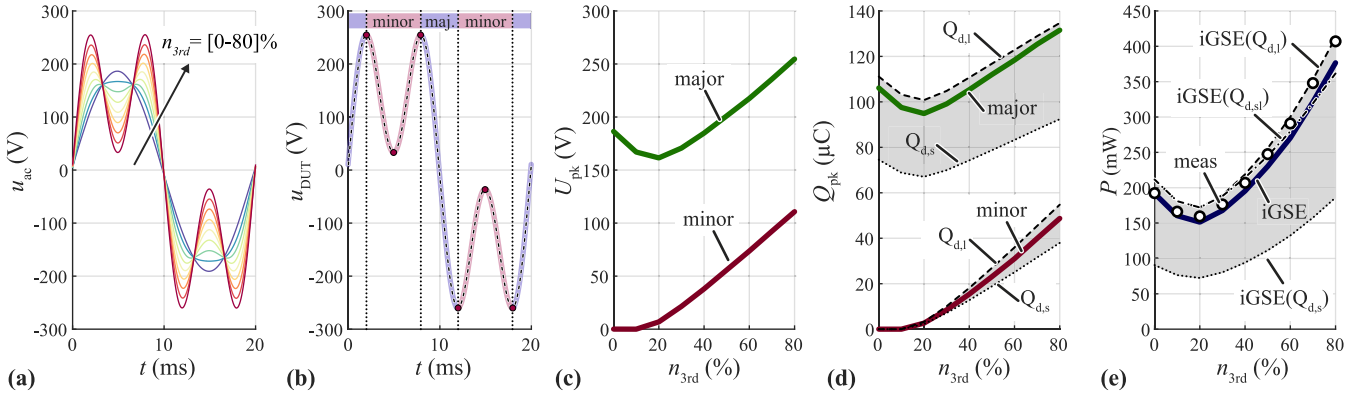


Fig. 9. Measurements under third harmonic injection conditions to validate the proposed Improved Generalized Steinmetz Equation for CCs (iGSE-C) modeling approach for nonsinusoidal voltage waveforms. (a) Measured excitation voltage waveforms with the third harmonic injection of variable magnitude (n_{3rd}) superimposed upon the 50 Hz, 150 V_{rms} fundamental voltage excitation. For $n_{3rd} > 20\%$, minor loops result [the splitting of major and minor loops is highlighted for $n_{3rd} = 80\%$ in (b)]. (c) Measured peak voltage amplitude U_{pk} of major and minor loops over n_{3rd} , as well as the calculated charge from the large-signal ($Q_{d,l}$) and small-signal ($Q_{d,s}$) differential capacitance curves of Fig. 15. (d) Measured peak charge amplitude Q_{pk} of major and minor loops over n_{3rd} , as well as the calculated charge from the large-signal ($Q_{d,l}$) and small-signal ($Q_{d,s}$) differential capacitance curves of Fig. 15. (e) Measured (scatter points) and calculated losses from (8) and (5) based on the measured charge (iGSE) or based on the calculated charge from the large-signal (iGSE($Q_{d,l}$)) and small-signal (iGSE($Q_{d,s}$)) differential capacitance curves of Fig. 15, or with the hybrid approach using large- and small-signal capacitance (iGSE($Q_{d,sl}$)) for each loop separately (cf., Section V-A). Accuracy between measured and calculated losses is within 7.6% when using the measured charge.

CISPR class A, making the high-frequency noise negligible at the DUT and supporting a variable-magnitude third harmonic injection. A fixed fundamental 150 V_{rms}, 50 Hz sinusoidal excitation is applied to DUT and the third harmonic component is gradually increased from 0% to 80% of the fundamental amplitude, as shown in Fig. 9(a).

With the linear loss dependence on frequency ($\alpha = 1$) found in Section IV-A, the integral term in (8) simplifies to twice the peak charge excitation magnitude Q_{pk} and the equation collapses to (7) for each loop. The losses can be straightforwardly calculated with (5) using major and minor loop splitting. In Fig. 9(b), an example of this major and minor loop splitting is shown for $n_{3rd} = 80\%$, with the peak voltage U_{pk} in each harmonic loop shown across the tested n_{3rd} values in Fig. 9(c).

2) *Measured Results*: With the SE parameters defined and the iGSE-C modeling known, the final step in predicting losses under nonsinusoidal excitations is to determine the correct peak stored charge, Q_{pk} , to use in (7). Fig. 9(d) shows three methods of estimating the charge in each loop: the directly measured charge (solid lines), the charge calculated from the large-signal differential capacitance ($Q_{d,l}$), and the charge calculated from the small-signal differential capacitance ($Q_{d,s}$). The large- and small-signal predictions are necessary for extensibility to arbitrary excitation waveforms and voltages, but we see that these two predictions differ widely in charge estimation, and, therefore, in loss prediction, with the large-signal $Q_{d,l}$ overestimating stored charge and the small-signal $Q_{d,s}$ underestimating the measured charge. This discrepancy—and an appropriate technique to estimate charge from an arbitrary voltage waveform—is investigated in depth in Section V.

Fig. 9(e) shows the calculated losses under third harmonic injection conditions with these different charge calculations, with a maximum error of 7.6% between the measured and calculated losses using the proposed iGSE-C modeling with the measured charge. At low harmonic injection magnitudes, the

voltage waveforms consists of a single major loop with decreasing peak amplitude, resulting in a decrease in measured losses. Above 20% harmonic injection, two identical minor loops start to appear. For $n_{3rd} > 20\%$, the peak charge of the major loop starts to increase again, thereby increasing the measured and predicted losses.

While the agreement between the measured losses and predicted losses constitute a validation of the proposed iGSE-C loss modeling approach, the estimation of peak charge is again seen to be fundamental to the *a priori* loss prediction in Fig. 9(e). This figure highlights the discrepancy in SE loss estimation between using the measured charge (excellent accuracy, denoted as *SE*), the calculated large-signal differential capacitance $C_{d,l}$ curve [again fairly accurate, *SE*($Q_{d,l}$)], and the calculated small-signal differential capacitance curve $C_{d,s}$ [significant underestimate of losses, *SE*($Q_{d,s}$)]. In Section V, we propose a hybrid approach that calculates the large- and small-signal capacitance for each loop separately ($Q_{d,sl}$) and gives the most accurate and extensible results to estimate peak charge and, therefore, to predict losses [cf., Fig. 9(e)].

C. Impact of DC Bias

For magnetic materials, a dc pre-magnetization has a significant impact on the losses [34] that is not captured by the iGSE. To overcome this shortcoming, Muhlethaler *et al.* [35] provided Steinmetz Premagnetization Graphs (SPGs) for several magnetic materials to quantify the dependency of the Steinmetz parameters on the pre-magnetization current bias. Naturally, and especially with the well-known voltage dependence of X7R capacitors [as measured for the DUT in Fig. 2(d)], the impact of a dc voltage offset on the CC losses must be investigated. We find here that the dc bias has no impact on the charge-loss relation found in Section IV-A, and that the same SE parameters can be employed to calculate the losses with a dc bias.

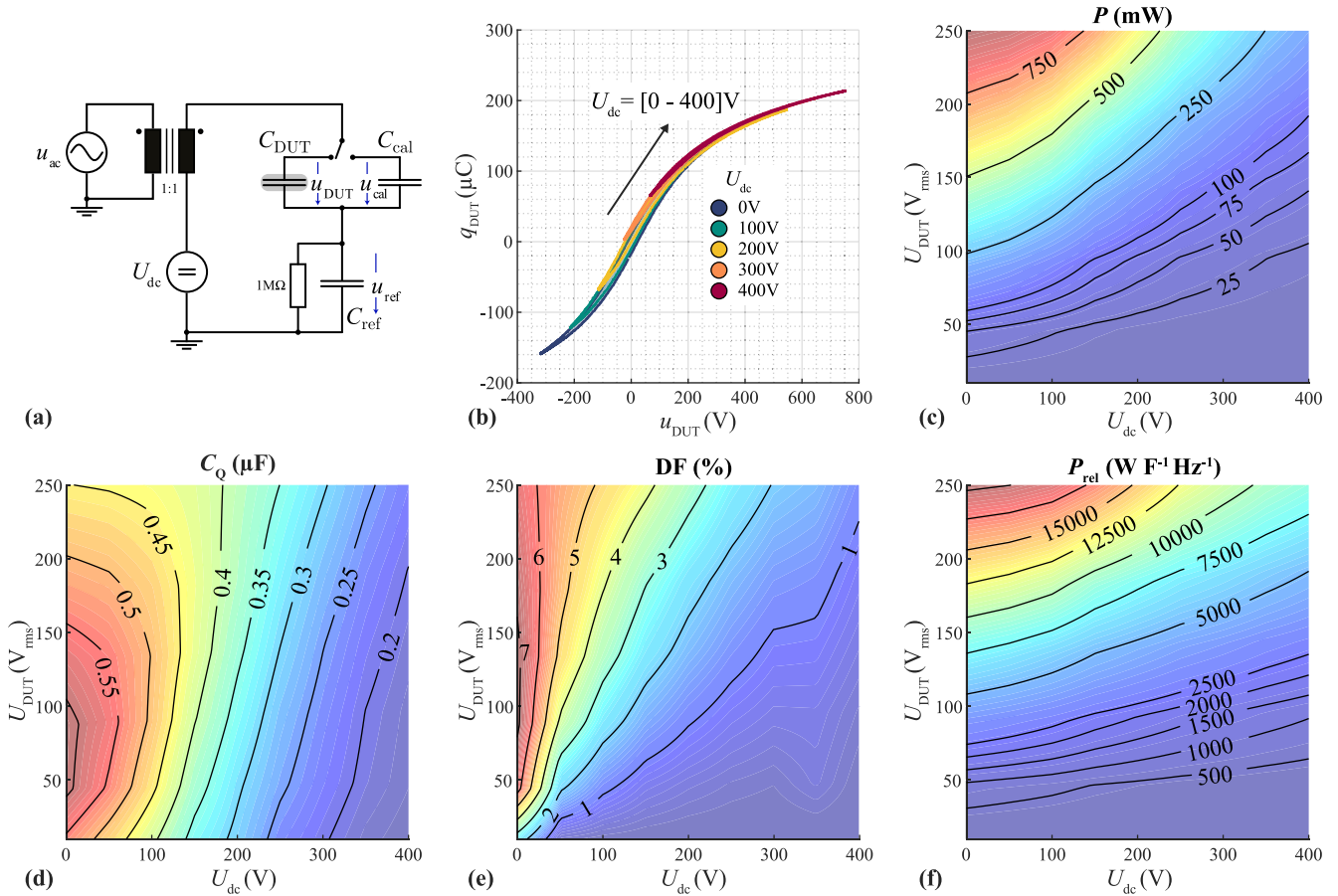


Fig. 10. Measured losses with varying dc bias and ac excitation voltage in the X7R CC under test (frequency fixed at 100 Hz for all measurements). Increasing dc bias decreases the losses in the DUT but simultaneously decreases the effective capacitance. Under the proposed charge-based SE loss model, dc bias has no impact on losses if peak charge is held constant (see Fig. 11). (a) Schematic circuit of a ST measurement setup with ac voltage excitation and dc voltage bias. All measurements are conducted with an ac frequency of 100 Hz. The employed components are given in Table II. (b) Measured hysteresis curves for constant ac amplitude of 250 V_{rms} and increasing dc bias from 0–400 V. Due to the parallel resistor of the reference capacitor, only the ac charge can be evaluated. As a function of ac voltage U_{DUT} and dc bias voltage, measured: (c) losses P , (d) charge-equivalent ac capacitance C_Q , (e) DF, and (f) losses P_{rel} normalized by measured ac capacitance and frequency, $P_{rel} = P/(C_Q \cdot f)$.

1) *Methodology*: The ST circuit of Fig. 5(a) is modified slightly, as shown in Fig. 10(a), to add a variable dc bias to the DUT. The dc bias source U_{dc} is referenced to protective earth with the ac excitation (from the ac power source) applied on top with an insulating transformer. A 1 MΩ resistor is added across the reference capacitor to ensure that the whole dc bias is applied to the DUT (otherwise, the dc voltage sharing is only defined by the capacitor leakage currents and the passive voltage probe resistances, i.e., poorly controlled parameters). As a result, only the ac charge excitation is captured by the ST measurement, and the dc charge offset is added by integrating the previously-measured (in Section IV-A) large-signal differential capacitance to the dc bias voltage. The dc bias is varied from 0–400 V with ac excitations at 100 Hz from 0 to 250 V_{rms}.

2) *Measurement Results*: Fig. 10(b) shows the measured hysteresis curves for a constant ac excitation voltage of 250 V_{rms} and a dc bias increased in 100 V increments from 0 to 400 V. With a positive bias, the hysteresis becomes nonsymmetric due to the voltage-dependent nonlinearity of the capacitor. The peak-to-peak charge excitation shrinks with increasing dc bias, especially

when the large-signal polarization around 0 V is avoided, and consequently both the losses and the large-signal capacitance (C_Q) decrease.

Fig. 10(c)–(f) shows contour maps of measured losses, large-signal capacitance, DF, and normalized losses across varying excitation magnitude (U_{DUT}) and dc bias (U_{dc}). Fig. 10(c) shows the measured losses, with the zero dc bias results (along the y-axis) matching the results of Fig. 7(a.ii) with a maximum of 823 mW. As expected from the curves of Fig. 10(b), the hysteresis area and the losses drop with increasing dc bias for a given ac excitation.

The large-signal capacitance also decreases with increasing dc bias, as shown in Fig. 10(d). The maximum ac capacitance is shifted toward higher ac amplitudes as the dc bias is increased, with the maximum occurring only when the curve encloses a voltage zero-crossing that results in large-signal polarization (explored in depth in Section V). Fig. 10(e) shows the DF, which continuously decreases with increasing dc bias (for a given excitation magnitude). We then find that a dc-referenced filter structure with a dc bias voltage and strictly positive capacitor

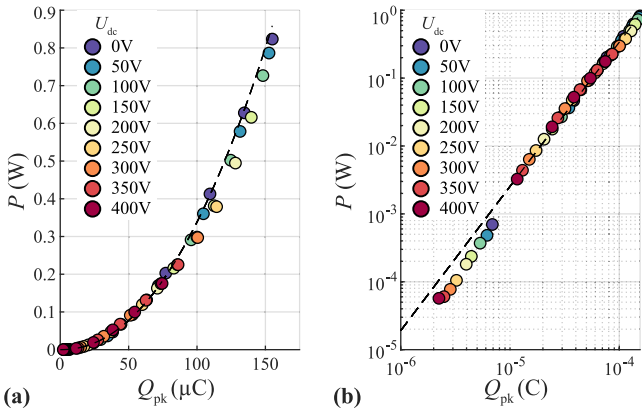


Fig. 11. Measured losses, from Fig. 10 c, plotted against measured charge Q_{pk} for 100 Hz AC frequency, AC voltages from 50 V_{rms} to 250 V_{rms} , and dc bias from 0 V to 400 V. Dotted lines are derived Steinmetz parameters ($k = 1.06 \cdot 10^6$, $\alpha = 1$, and $\beta = 2.12$) in (7), which show excellent agreement with the measured data even under dc bias. The same Steinmetz fitting holds under dc bias conditions, indicating that the losses in the DUT are not dependent on dc bias, unlike in magnetic components. (a) Linear representation and (b) logarithmic representation.

voltages (cf., Fig. 1) would yield lower overall losses than a filter with zero dc bias, although more parallel capacitors would need to be employed to achieve the same effective capacitance value.

To visualize this tradeoff between losses (improving with dc bias) and capacitance (decreasing with dc bias), Fig. 10(f) normalizes the losses by ac capacitance and frequency, allowing a direct comparison of filter losses for an effective capacitance requirement. For a given ac excitation amplitude, the losses are either relatively constant across dc bias or decrease slightly at higher excitation amplitudes (where the zero crossing can be avoided with a large dc bias). We return to the Steinmetz fitting to more rigorously assess the effect of dc bias on losses and capacitance.

3) *Steinmetz Fitting*: The measured losses across dc bias from Fig. 10(c) are scattered against the Steinmetz excitation parameter of (7), Q_{pk} (which is here derived from the charge-equivalent ac capacitance C_Q and U_{DUT}) in Fig. 10(d), in both linear [see Fig. 11(a)] and logarithmic [see Fig. 11(b)] scales. The scatter color represents the dc offset voltage. The same Steinmetz fitting from Section IV-A ($k = 1.06 \cdot 10^6$, $\alpha = 1$, and $\beta = 2.12$) is plotted as a dotted line in each plot.

Fig. 11 clearly shows that the losses still follow the identical power law fit obtained from the ac-only measurement results, with discrepancies again only evident for loss magnitudes below 1 mW. In contrast to magnetic materials, the dc bias has no impact on CC losses for a given charge excitation amplitude in the considered frequency range. While the bias has a major impact on the differential capacitance, as shown in Fig. 10(c), only the charge magnitude is needed to calculate losses. This greatly simplifies the loss modeling of CCs and again validates the proposed charge-based SE and iGSE-C approaches.

D. Impact of Temperature

Thus far, short measurement times were used to maintain the DUT near room temperature (25° C) and measure consistent

loss data, but with [14] showing that the losses of X7R CCs are highly temperature dependent, the impact of temperature on the measured and modeled losses needs to be evaluated.

1) *Methodology*: To assess the impact of temperature on losses, the DUT capacitor is now allowed to self-heat with a long measurement time. The measurement results from Section IV-A revealed losses of 9 mW/Hz or a loss density of 69 mW/Hz/cm³ at the maximum excitation voltage of 270 V_{rms} , and, hence, substantial capacitor heating is expected.

Electrical (via the ST circuit) and thermal measurements (via a high-frame rate thermal camera, the FLIR A655sc) are recorded simultaneously. Voltages are recorded with a large-memory oscilloscope, with memory sufficient to record 28s of data with losses on an individual cycle basis extractable in postprocessing (tests were stopped after 28s or if the DUT reached 90°C). To synchronize the electrical and thermal measurements, we assume a small thermal capacitance (C_{th}) of the DUT and align the oscilloscope trigger with the first increase of temperature. Similarly, the turn-OFF of the electrical source and the peak temperature happens simultaneously (noting that the device does not reach thermal steady state in any of our test conditions), providing another synchronization verification. The excitation voltage is fixed at 270 V_{rms} and the frequency is varied from 100 to 500 Hz with 100 Hz steps.

To provide a secondary loss verification with temperature, additional short-pulse (no self-heating) measurements (similar to Section IV-A) are recorded with the DUT fixed to a heating plate at variable temperature. These losses are recorded at 500 Hz.

2) *Measurement Results*: The recorded temperature and measured losses across elapsed time are shown in Fig. 12(a)–(b), with the short-duration hot-plate measurements overlaid as scatter points. These short-pulse measurements are close to, but constantly slightly below, the losses measured in the transient measurement, which can be explained by the unavoidable self-heating implicit in the short-duration tests that shifts the real dielectric temperature slightly higher. The losses near $t = 0$ s are close to the measured results and Steinmetz predictions of Section IV-A. Overall, these verifications indicate both that the synchronization is accurate and the temperature-dependent losses can be accurately measured under transient conditions.

Measured losses (normalized to the room-temperature value), large-signal capacitance, and DF are plotted with respect to temperature in Fig. 12(c)–(e). We observe that both losses and effective capacitance drop substantially with increasing temperature (also shown in [14]), with losses declining faster than capacitance and DF, therefore, declining at higher dielectric temperature.

While the charged-based SE parameters for CCs do not depend on dc bias, these results indicate that operating temperature is an important factor that must be considered for loss prediction. In Fig. 12(c), for example, the dashed line of best fit is plotted to represent the change of losses as $P_{rel}(T) = 1 - 0.58\%/K \cdot (T - T_0)$ (with $T_0 = 20.28^\circ\text{C}$). At high temperatures, the room-temperature SE parameters overpredict the measured losses by a maximum of 15%, as shown with the dotted line in Fig. 12(c). This indicates two separate temperature-related effects: first, the decrease in charge-equivalent capacitance with increasing temperature [see Fig. 12(d)] results in lower predicted losses

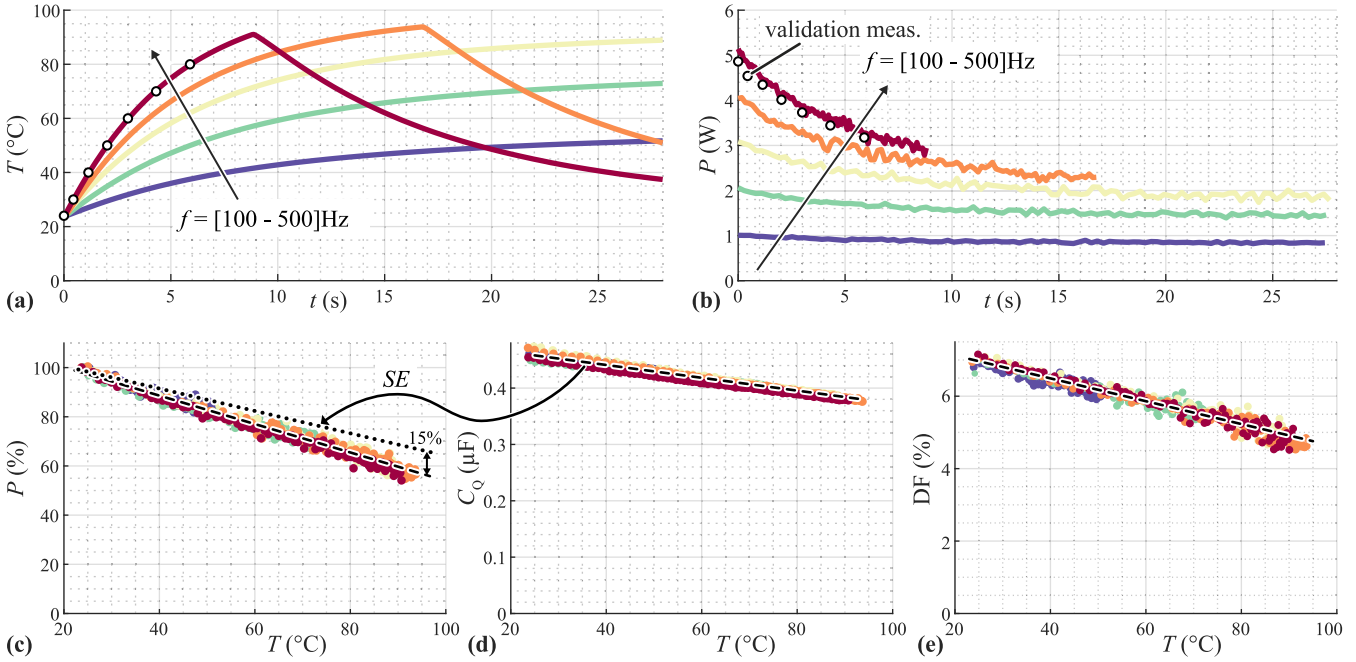


Fig. 12. Electrically measured losses under transient conditions with varying DUT temperature and excitation frequency from 100 to 500 Hz (excitation magnitude fixed at 270 V_{rms} for all measurements). Scattered circles show measurements without self-heating (a hot-plate was used to control the device temperature and short-pulse measurements, like those reported in Section IV-A, were conducted), which match the transient measurements closely and validate the methodology. Losses and effective capacitance decrease with temperature, but losses decrease faster than C_0 and DF therefore decreases. (a) Measured DUT temperature and (b) losses over time for a constant ac voltage $U_{ac} = 270$ V_{rms} and increasing frequency f from 100 to 500 Hz. Scatter points show hot-plate measurements to validate the transient method. (c) Losses relative to the initial value at room temperature (25° C), (d) measured large-signal capacitance, and (e) DF as a function of temperature T . The decrease of charge-equivalent capacitance in (d) reduces the SE-predicted losses to those shown by the dotted line in (c), with a maximum overestimation of 15% over the measured losses at high temperature.

based on lower Q_{pk} [the SE line in Fig. 12(c)], but there appears to be an additional change to the dielectric loss mechanism with temperature that accounts for an additional 15% of loss reduction. This discrepancy could eventually be obviated by means of an SE coefficient $k(T)$ that scales linearly with temperature, but with a small resulting deviation, this is not further considered.

3) *Transient Calorimetric Capacitor Loss Measurement*: This article was originally motivated by unexpectedly high filter capacitor losses in an existing converter prototype. In these existing systems, an ST circuit cannot be directly employed and the designer may be seeking to select the optimal filter capacitor or quantify the losses. From transient calorimetric techniques (e.g., [36]), we know that the device temperature and device losses are linked by the thermal resistance R_{th} and thermal capacitance C_{th} , and fitting these to the loss measurements of Fig. 12 may enable *in situ* calorimetric loss measurements. This transient technique is introduced here and again used for two filter capacitors in Section V.

To perform an *in situ* transient loss measurement [see Fig. 13(a)], the following procedure is followed.

- 1) The temperature rise of the capacitor $T(t)$ is recorded with a high frame rate thermal camera (if the DUT is not accessible with a thermal camera, a temperature sensor can be used) for an operating point where the losses are known across temperature. Here, we use the 100 Hz excitation of Fig. 12(a), but any previously recorded low-frequency excitation is a good candidate.

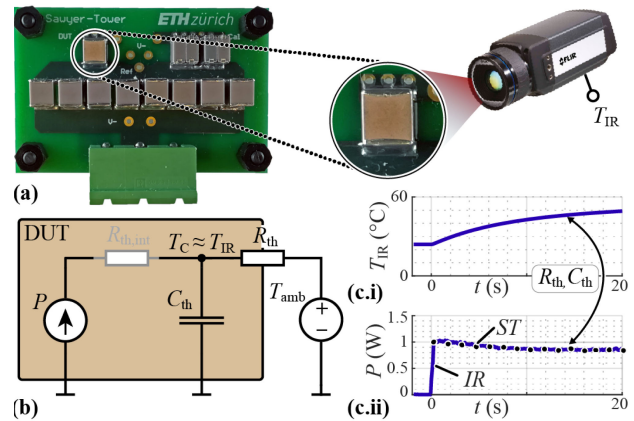


Fig. 13. Illustration of an *in situ* transient calorimetric capacitor loss measurement approach: (a) ST circuit with highlighted DUT CC and FLIR A655sc thermal camera. (b) simplified thermal equivalent circuit of the DUT where the internal thermal resistance $R_{th,int}$ is assumed to be negligible, (c.i) recorded temperature curve from Fig. 12(a) ($f = 100$ Hz) and (c.ii) calculated capacitor losses with $R_{th} = 34.96^\circ\text{C}/\text{W}$ and $C_{th} = 0.325\text{Ws}/^\circ\text{C}$.

- 2) With the equivalent thermal circuit of Fig. 13(b), and assuming $R_{th,int}$ is negligible, the equivalent thermal resistance R_{th} and thermal capacitance C_{th} are extracted from the temperature curve as

$$P(t) = C_{th} \cdot dT(t)/dt + \frac{T(t) - T_{amb}}{R_{th}}. \quad (14)$$

For the measurement results in Fig. 12(a) and the ST setup of Fig. 13(a), the thermal resistance and capacitance are fitted as $R_{th} = 34.96^\circ\text{C}/\text{W}$ and $C_{th} = 0.325\text{Ws}/^\circ\text{C}$. Fig. 13(c.i) shows the recorded temperature curve from Fig. 12(a) for $f = 100\text{ Hz}$, and in Fig. 13(c.ii), we see that the calculated capacitor losses with (14) and the measured $T(t)$ are in good agreement with the electrically measured (using the ST circuit) losses in Fig. 12(b).

Note that both R_{th} and C_{th} are determined by the particular physical environment in which the capacitor is installed, and must be determined on a setup-by-setup basis. We show the application of this transient prediction method in Section V.

E. High Frequency (HF) Excitation

Finally, as a filter component in a switched-mode converter such as in Fig. 1, the CCs will necessarily see switching frequency harmonics. The losses from this high-frequency waveform component must be understood as well, and we seek to characterize the losses in the DUT from 1 to 100 kHz.

1) *Methodology*: Measuring these high-frequency losses across the large capacitances studied here introduces additional difficulties and a minor reconsideration and recalibration of the measurement setup (note that prior high-frequency ST measurements measured capacitances of the, at most, nF order, not the 100 nF order studied here [25], [26]). From Fig. 2(a), we see that the DUT impedance is now in the range of Ω , and, according to the DF measurement of Fig. 2(c), this places the ESR in the range of $10\text{m}\Omega$, which is of the same order as the contact resistance of the solder joints and connection paths. Furthermore, the current, which increases linearly with frequency, is several orders of magnitude higher than in Section IV-A, making the control of the resistive losses critical.

If the reference capacitor and calibration capacitor are considered lossless and $C_{ref} \approx 10 \cdot C_{cal}$, as in Section IV-A, equal contact resistance for both capacitors causes the apparent loss tangent of the reference capacitor to be ten times larger than that of C_{cal} , giving a *negative* loss reading for the calibration and also deteriorating the measurement with the DUT. Minimizing the return path impedance is, therefore, crucial and has to be verified with a calibration measurement. For the high-frequency measurements, it is preferred to have similar capacitance magnitudes between C_{ref} and the DUT to overcome this issue and to allow a calibration measurement with close to identical currents as in the DUT evaluation, and C_{cal} is implemented with one $0.2\ \mu\text{F}$ (TDK, CAA572C0G2J204J640LH) and two $0.15\ \mu\text{F}$ (TDK, C5750C0G2A154J230KE) C0G capacitors, yielding a total capacitance of 500nF , which is equal to the DUT under small-signal conditions. (Note that one alternative is measuring a capacitor with the same dielectric but less capacitance, which simultaneously increases the impedance and ESR and can be selected to again make the ESR much greater than the contact resistances. This approach was not selected here because the exact realization of the dielectric is not known with commercial devices.)

Excitations of 5, 7.5, and 10 V_{rms} are applied to the DUT, with the magnitude limited by the total losses, which scale with frequency. A sinusoidal excitation is applied with a high-frequency power amplifier up to 100 kHz, and, to validate that $\alpha = 1$ holds

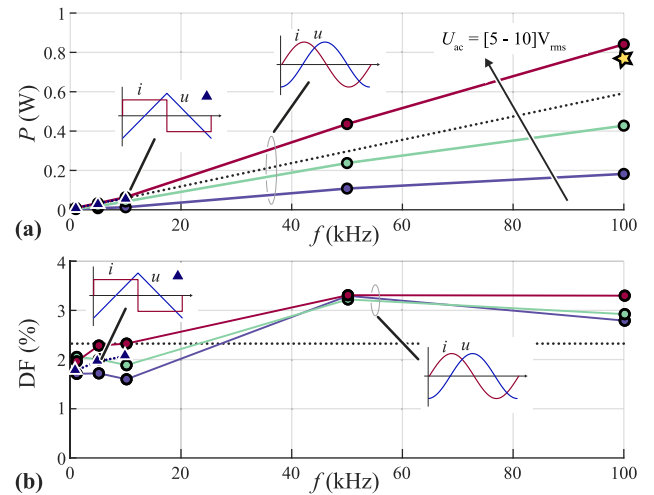


Fig. 14. Measured losses at high-frequency in the CCs DUT from 1 to 100 kHz with an excitation voltage of 5, 7.5, and 10 V_{rms} . Losses are identical between triangular (measurement indicated with triangular scatter points) and sinusoidal (indicated with round scatter points) excitations with the same peak voltage, as expected by the SE fitting of $\alpha = 1$. Triangular waveform measurements are limited by the power amplifier bandwidth to 10 kHz. (a) Measured losses and (b) DF. Star scatter point shows thermally measured losses using (14), which validates the high-frequency ST measurements.

at high frequency, a triangular voltage (rectangular currents) excitation of 10 V_{rms} is also applied. The triangular waveform is limited to 10 kHz by the bandwidth of the high-frequency power amplifier.

2) *Measurement Results*: Fig. 14 shows the measured high-frequency losses under the triangular and sinusoidal voltage excitations. The DF for 10 V_{rms} is relatively flat (above 2%) up to 10 kHz and increases to 3.3% at 100 kHz for losses of 860 mW. As expected with $\alpha = 1$, the losses for triangular voltages and sinusoidal voltages with the same peak ac voltage are identical, as shown in Fig. 14(a). A transient thermal measurement is performed to validate the high-frequency ST measurements, where using (14) and the previously derived R_{th} and C_{th} values, we find losses of 787 mW at 100 kHz [represented by the star scatter point in Fig. 14(a)].

These measurements provide a loss estimation for the high-frequency component in the filter capacitors. The measured DF does not change substantially when moving to the kHz range, with a small increase for higher excitation amplitudes. The effect of dc bias on the high-frequency losses was not considered, although recent research indicates a bias dependence for CC losses above 75 kHz [37]. Even under the assumption of constant SE parameters at high frequency, there is excellent matching between the calculated and calorimetrically measured losses in a practical application, as we show in the following section. In this section, we combine the high-frequency and low-frequency loss modeling approaches to provide guidelines to estimate CC losses in a switched-mode converter application.

V. GUIDELINES FOR CONVERTER LOSS ESTIMATION

We again return to the analogy of ferromagnetics to highlight the challenges unique to ferroelectric CCs. In a converter such

as in Fig. 1, the inductive components are subject to both low-frequency (typically sinusoidal and near line-frequency) current imposed by the control system and a high-frequency current ripple due to the PWM operation of the power semiconductors. Because these two frequencies are separated by multiple orders of magnitude, the loss contributions are typically considered separately and in most practical applications, the low-frequency core losses are small [38]. The high-frequency magnetic flux is determined easily by integrating the applied voltage-time area, but the losses for a given excitation are dc-bias dependent and SPGs are required to calculate the high-frequency core losses [35]. As gapped inductors are designed with sufficient margin to the saturation flux density of the core (to avoid a sudden roll-off of the inductance value), they feature an almost constant inductance value throughout the eligible current range and, hence, the premagnetization can easily be calculated [39]. In summary, with known SE parameters and SPGs, the assessment of core losses is relatively straightforward.

As previously presented, the capacitors of the sine-wave filter in the converter of Fig. 1 also face a low-frequency voltage excitation and a high-frequency voltage ripple due to the PWM operation of the power semiconductors. To use the presented iGSE-C approach with ferroelectric capacitors, the charge excitation must be known, which for the high-frequency excitation can be obtained directly by integrating the high-frequency inductor current ripple. Assuming the Steinmetz parameters are independent of dc bias (shown in Section IV-C for low frequencies up to 250 Hz) for high frequencies as well, the high-frequency losses are straightforward to assess and are relatively minor in sine-wave filters with a large fundamental voltage swing and low high-frequency voltage ripple. In contrast to magnetic materials, however, the fundamental frequency losses in the CCs are substantial, as shown in this article. For a given voltage, the charge excitation depends on the nonlinear relative permittivity (or differential capacitance), and with the SE and iGSE-C modeling dependent on the peak charge stored, the correct estimation of this charge is critical to obtain an accurate loss calculation. According to Fig. 2(d), the differential capacitance of the DUT reduces by approximately 70% for a dc bias of 400 V, and the nominal operating regime includes, essentially, substantial saturation, which further complicates the charge estimation. This charge estimation is the focus of the following section.

A. Evaluation of the Charge Excitation

For a given capacitor voltage excitation $U(t)$, the charge is defined by the differential capacitance C_d as

$$Q(t) = \int C_d(U) \cdot \frac{dU(t)}{dt} dt = \int C_d(U) dU. \quad (15)$$

With the highly nonlinear C_d found in Section IV-A, the small-signal C_d curve in Fig. 2(d) is only true under small-signal excitation conditions. Otherwise, $C_d(U)$ must be back-calculated using (6) under the large-signal excitations. From Fig. 10 and the discussion around those results, we can already see that multiple $C_d(U)$ functions must exist that depend on the excitation magnitude and the dc bias. The extracted $C_d(U)$

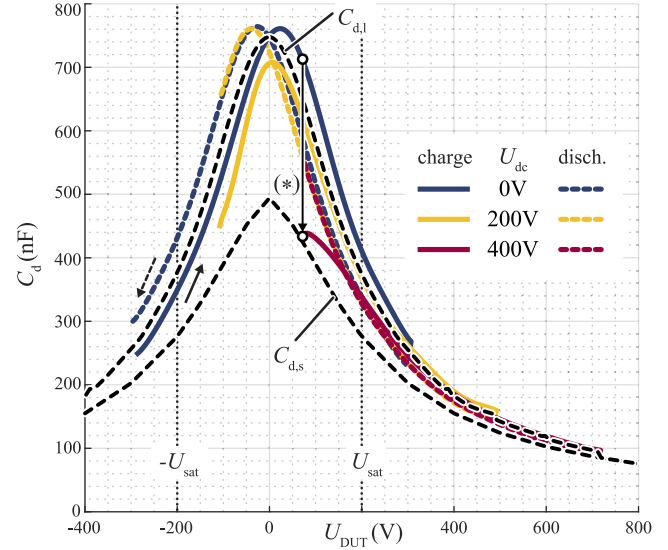


Fig. 15. Differential capacitance over voltage derived according to (6) for the measured hysteresis curves shown in Fig. 10(b) with 250 V_{rms} ac excitation and increasing dc bias of 0, 200, and 400 V. The differential capacitance is shown for the charging (solid) and discharging (dotted) portions of the voltage excitation. For a given voltage, C_d depends greatly on the overall hysteresis waveform, including the ac magnitude, dc bias, and direction of the excitation [see (*), which highlights the variability near 0 V]. The small-signal $C_{d,s}$ and large-signal $C_{d,l}$ differential capacitance curves can be used to estimate the charge excitation for small or large ac voltage excitations, respectively.

from the excitations in Fig. 10(b) are plotted in Fig. 15 for $U_{ac} = 250$ V_{rms} and dc bias voltages of 0, 200, and 400 V (in the plot, we exclude regions where dQ/dt or dV/dt are close to zero to avoid poor signal-to-noise ratios).

First, we see a large dependence of differential capacitance both with dc bias U_{dc} and with the direction of the excitation (charging or discharging) in Fig. 15. The (*) highlights that the C_d close to the zero-voltage crossing greatly depends on both the dc bias and the overall path of the hysteresis loop. In contrast, if the charging signal exceeds U_{sat} , the associated discharging C_d is, for the most part, largely independent of dc bias and ac magnitude. (The same holds true if the discharging curve exceeds $-U_{sat}$, with identical charging curves.) For the $U_{dc} = 400$ V excitation, the capacitor voltage never changes sign, and the large-signal polarization is not fully relaxed when the minimum voltage is approached. The ensuing “non-switching transition” [40] (where the voltage polarity never reverses) results in a low differential capacitance C_d .

The nonlinearity of the capacitance around the zero-voltage crossing, then, complicates the prediction of the stored charge for a given voltage waveform, as the integration in (15) is not straightforward. For large ac excitation magnitudes, Q can instead be conservatively approximated with the large-signal capacitance as the average of C_d during the rising and falling voltage excitations, as shown in Fig. 15 with the $C_{d,l}$ dashed line. This curve is a good approximation when the ac swing exceeds $|U_{sat}|$ on both the negative and positive voltage swings. $C_{d,s}$ remains a valid prediction of charge storage under small-signal excitations.

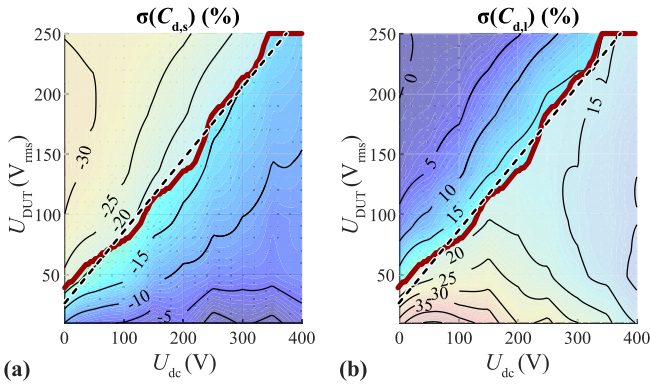


Fig. 16. Relative error σ of the calculated charge-equivalent capacitance $C_{Q,\text{calc}}$ using (15) for sinusoidal ac excitation and dc bias relative to the measured C_Q of Fig. 10(d) with (a) the small-signal $C_{d,s}$ and (b) the large-signal differential capacitance $C_{d,l}$ (cf., Fig. 15) models. The red line indicates the boundary between the regions where the small- and large-signal approximations are, respectively, preferred to minimize the charge approximation error.

For an arbitrary waveform, including those with the third harmonic injections of Fig. 9(a), the charge in a given loop can be calculated with either $C_{d,s}$ or $C_{d,l}$, which respectively yield the lower and upper bounds on hysteretic losses, as shown in Fig. 9(d) and (e). Neither prediction method of charge from a given voltage waveform, however, is perfect, and there remains the question of exactly what voltage magnitude constitutes a small- or large-signal excitation.

A comparison of the resulting charge approximation error (σ) using $C_{d,s}$ and $C_{d,l}$ for the measured charge in Fig. 10(d) is shown in Fig. 16. As expected, the small-signal charge prediction $C_{d,s}$ is a good approximation when the ac magnitude is small absolutely or relative to the dc bias [cf., Fig. 16(a)], while the opposite holds true for the prediction given by $C_{d,l}$ [cf., Fig. 16(b)].

The regions where the small- and large-signal approximation, respectively, yield the minimal absolute charge error $|\sigma|$ are separated by the red line U_{bound} in Fig. 16, which can be simplified as (the dashed lined in Fig. 16)

$$U_{\text{bound}} = 0.60 \cdot U_{\text{dc}} + 26.35\text{V}. \quad (16)$$

For a minimal charge approximation error at a given dc bias U_{dc} , C_d is selected as

$$C_d = \begin{cases} C_{d,s}, & U_{\text{DUT,rms}} \leq U_{\text{bound}} \\ C_{d,l}, & U_{\text{DUT,rms}} > U_{\text{bound}} \end{cases} \quad (17)$$

yielding a maximal charge approximation error of $|\sigma_{\text{max}}| = 20\%$ across the full dc bias and ac magnitude sweep. With minor loops for nonsinusoidal excitations, (16) should be employed for each loop separately, as shown in Fig. 9(e).

This charge estimation approach—necessitated by the non-linear ferroelectric characteristics, and especially by the large-signal polarization near 0 V—could be avoided by designers with two potential alternatives. Once the SE parameters have been derived for a given DUT, the losses can be calculated based solely on a charge measurement (e.g., using a current probe and integrating charge) when the device is excited with the desired fundamental frequency waveform. (Note that this method is

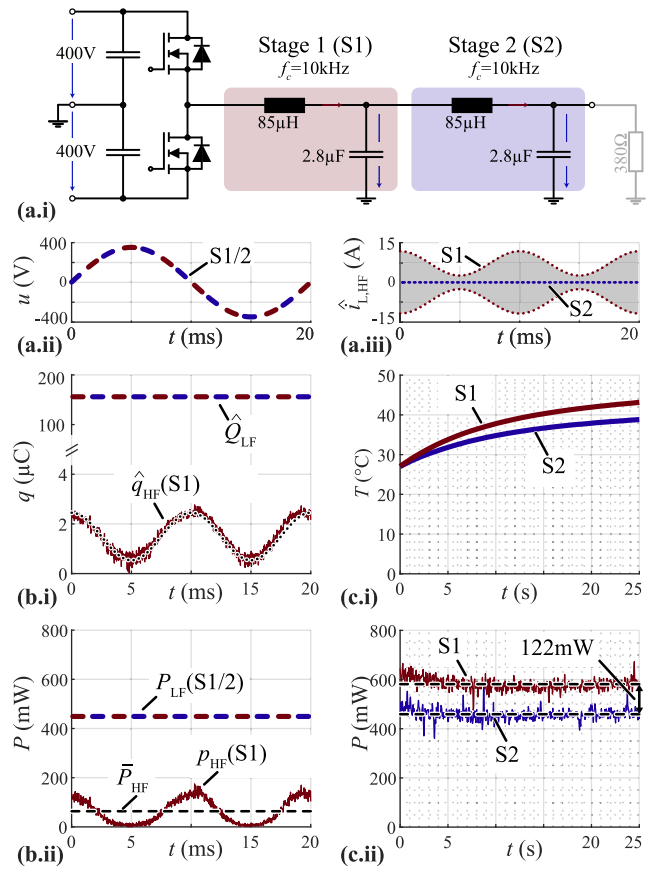


Fig. 17. (a.i) Example of single-phase dc–ac converter with a split 800 V dc-link and a 50 Hz, 250 V_{rms} ac voltage. The output sine-wave filter consists of two identical filter stages, where only the first filter stage S1 is subject to a substantial high-frequency excitation. Calculated (a.ii) low-frequency ac voltage waveforms of the capacitors in S1 and S2 and (a.iii) calculated high-frequency envelope of the S1 inductor current. (b.i) Measured (solid line) and calculated (dashed line) low-frequency charge excitation of S1 and S2 as well as the time-varying high-frequency charge waveforms of S1. (b.ii) Calculated low-frequency and high-frequency capacitor losses using the measured charge excitation and the SE parameters from Section IV-A. (c.i) Measured capacitor transient temperature curves of S1 and S2 during converter operation. (c.ii) Calculated capacitor losses (average values represented as dashed lines) from the transient thermal measurements of (c.i) with (14) and the thermal equivalent circuit parameters from Section IV-D.

difficult to use to *determine* the SE parameters, as discussed in Section III.) Alternatively, manufacturers could provide (in addition to SE parameters) online tools for hysteresis modeling based on their physical knowledge of polarization effects in commercial dielectrics.

B. Design Example

Finally, we employ the tools and measured losses here to calculate the total losses of CCs in a single-phase dc–ac converter with a split 800 V dc-link and a 50 Hz, 250 V_{rms} ac voltage [shown in Fig. 17(a.i)]. The switching frequency is selected at $f_s = 100$ kHz and a two-stage filter (comprised of two identical filters, S1 and S2, with a crossover frequency $f_c = 10$ kHz) provides an attenuation of approximately 80dB at the switching frequency. Each filter is constructed with an inductor of

$L = 85\mu\text{H}$ and six paralleled DUT capacitors ($C = 2.8\mu\text{F}$). A load of 380Ω is used at the output.

The filter stages have a nearly identical fundamental-frequency voltage excitation [see Fig. 17(a.ii)], with the fundamental-frequency voltage drop across the inductor of $S1$ safely neglected. The peak high-frequency current ripple $\hat{i}_{L,\text{HF}}$ of the inductor in $S1$ can be calculated from the time varying duty cycle $d(t) = \frac{u_{\text{ac}}(t)}{\frac{1}{2}U_{\text{dc}}}$ pattern as

$$\hat{i}_{L}(t) = \frac{1}{8} \frac{U_{\text{dc}}(1-d)(d+1)}{Lf_s} \quad (18)$$

and reaches up to 12A in this application. In $S2$, the high-frequency current ripple is attenuated by an additional 40dB and is, therefore, negligible [see Fig. 17(a.iii)], yielding an opportunity to break apart the relative loss contributions from the low-frequency and high-frequency components.

According to (17), the low-frequency charge is best calculated using $C_{\text{d},1}$, with $\hat{Q}_{\text{LF}} = 159\mu\text{C}$ as the result. To validate this prediction, the filter capacitor of $S2$ was replaced with the ST setup, where a low-frequency peak excitation of $\hat{Q}_{\text{LF}} = 156\mu\text{C}$ was directly measured [cf., Fig. 17(b.i)].

The high-frequency charge excitation in $S1$ can be obtained by integrating the high-frequency inductor current of $S1$ and dividing the current by the six paralleled capacitors, giving a maximum per-device charge of $\hat{Q}_{\text{HF,max}} = 2.5\mu\text{C}$ [dotted line in Fig. 17(b.i)]. The measured switching-frequency charge ripple amplitude nicely follows this theoretical prediction.

Using the SE parameters from Section IV-A ($k = 1.06 \cdot 10^6$, $\alpha = 1$, $\beta = 2.12$), the low- and high-frequency losses for $S1$ and $S2$ can be calculated from the charge predictions above. In $S1$ and $S2$, the calculated line-frequency losses are 450 mW, and the time-varying high-frequency losses in $S1$ peak at 173 mW with an average value \bar{P}_{HF} of 64 mW [see Fig. 17(b.ii)]. The transient calorimetric measurement approach of Section IV-D is used to measure the losses (which cannot be accurately measured with the ST circuit with the low- and high-frequency excitations, as discussed in Section IV-E).

Fig. 17(c.i) shows the temperature rise of the capacitors, which is translated into instantaneous power loss [see Fig. 17(c.ii)] with (14) and the thermal equivalent circuit parameters from Section IV-D. The measured losses in $S2$ are 459 mW, predicted with an error under 2%. The high-frequency losses are indeed negligible in this stage. For the capacitor of $S1$, the measured losses increase by 122 mW over the losses in $S2$ due to the high-frequency ripple. While the prediction of \bar{P}_{HF} is OFF by approximately a factor of two (64 mW predicted losses), the prediction error of total losses in $S1$ is only 12%, and the high-frequency error can be partially explained by the reported increase of DF by 30% at high-frequency [see Fig. 14(b)]. Nonideal current sharing among the capacitors is also a potential error source.

Nonetheless, the high-frequency losses of 122 mW are only 20% of the overall losses, and clearly the low-frequency loss component dominates in CCs for the considered sine-wave filter with a small high-frequency voltage ripple compared to the

fundamental voltage waveform. For motor drives with fundamental frequencies up to 200 to 300 Hz, this ratio may be even more tilted toward the low-frequency losses. The total loss approximation error for $S1$ is under 12%, validating the measurements, the iGSE-C model, and the charge estimation approaches in this article.

VI. CONCLUSION

Ferroelectric Class II CCs promise large volume reductions in inverter and rectifier sine-wave filters, and are expected to gain importance in future applications demanding exceptional power density. While previous work has found nonlinear and large losses in these components, no extensible loss model is available in the literature that accurately describes these hysteretic losses.

In this article, a Steinmetz-based loss modeling approach—called the Improved Generalized Steinmetz Equation, or iGSE-C—is proposed and verified for a commercially available X7R CC. We measure the ferroelectric hysteresis losses across ac excitation magnitude, dc bias, frequency, temperature, and harmonic injection using the ST circuit.

Losses are shown to scale according to a power law with peak charge, with the Steinmetz coefficients constant over dc bias. By analogy with well-developed methods for ferromagnetic components in power electronics applications, the iGSE-C accurately predicts losses under nonsinusoidal voltage excitations, as long as the charge is accurately characterized or measured.

Finally, a procedure is given and validated for predicting total losses—the sum of low-frequency and high-frequency losses—in a sine-wave filter, with the low-frequency losses dominating the total power dissipation in the CCs.

APPENDIX A

CALORIMETRIC MEASUREMENT METHODS

A. Steady-State Calorimetric Measurement

A steady-state calorimetric measurement has the advantage that the fundamentally large ratio of reactive to active power has no impact on the measurement accuracy or precision, and these measurements were conducted with film capacitors for traction applications in [32]. With the strong temperature dependence of X7R CCs previously known [14], this technique is not possible here.

B. Indirect Transient Calorimetric Measurement

An indirect measurement uses the temperature increase of something *other than the DUT* to estimate the losses in the DUT. These losses are typically recorded under quasi-steady-state conditions. In [33], the dielectric losses of insulation materials were evaluated by measuring the increase in temperature of a thermally isolated test chamber (with a calibration resistor in an equal package). In [15], a similar approach was used, with the DUT located in an oil bath and the temperature increase measured. In [41] and [42], wide-bandgap-semiconductor switching losses were measured with the temperature increase of a brass block after a dc current calibration (the steep dv/dt -transients jeopardize any electrical measurement). While this

measurement technique produces valid, accurate results, it is much slower than the implemented electrically based technique.

C. Direct Transient Calorimetric Measurement

In order to rapidly evaluate semiconductor hard and soft switching losses, recently a new method was introduced where the temperature of the semiconductor case is measured directly (again after a dc current calibration step), reducing the measurement time to the range of seconds [36]. The same method was employed in [43] to characterize the losses of magnetic materials under large-signal excitations with frequencies up to 50 MHz. The calibration losses are generated by impressing a dc current upon the magnetic core samples.

The dc calibration (or any other known loss calibration) is not possible for capacitors, and, therefore, this method is not directly applicable here. Based on existing capacitor loss data, however, this method can be employed for an *in situ* measurement in a hardware prototype, as discussed in Section IV-D and demonstrated in Section V-B.

ACKNOWLEDGMENT

The authors would like to thank Prof. S. Ben-Yaakov for his useful feedback on the initial manuscript. Additionally, they would like to thank P. Papamanolis, Ph.D. Student at the Power Electronics Systems Laboratory (PES), ETH Zurich, and Dr. T. Guillod, Postdoctoral Researcher at PES, for highly interesting discussions and valuable inputs on loss modelling concepts and measurement techniques for magnetic materials. They would also like to thank N. Nain, M.Sc. Course Student at PES, for her extensive support in taking the initial measurements.

REFERENCES

- [1] C. B. Barth, T. Foulkes, I. Moon, Y. Lei, S. Qin, and R. C. N. Pilawa-Podgurski, "Experimental evaluation of capacitors for power buffering in single-phase power converters," *IEEE Trans. Power Electron.*, vol. 34, no. 8, pp. 7887–7899, Oct. 2018.
- [2] K. Raggl, T. Nussbaumer, and J. W. Kolar, "Guideline for a simplified differential-mode EMI filter design," *IEEE Trans. Ind. Electron.*, vol. 57, no. 3, pp. 1031–1040, Mar. 2010.
- [3] G. Buja and G. Indri, "Improvement of pulse width modulation techniques," *Arch. für Elektrotechnik*, vol. 57, no. 5, pp. 281–289, Sep. 1975.
- [4] D. O. Boillat, F. Krismer, and J. W. Kolar, "EMI filter volume minimization of a three-phase, three-level T-type PWM converter system," *IEEE Trans. Power Electron.*, vol. 32, no. 4, pp. 2473–2480, Oct. 2016.
- [5] Y. Lei *et al.*, "A 2 kW single-phase seven-level flying capacitor multilevel inverter with an active energy buffer," *IEEE Trans. Power Electron.*, vol. 32, no. 11, pp. 8570–8581, Jan. 2017.
- [6] D. Bortis, D. Neumayr, and J. W. Kolar, " $\eta - \rho$ -Pareto optimization and comparative evaluation of inverter concepts considered for the Google Little Box Challenge," in *Proc. 17th IEEE Workshop Control Model. Power Electron.*, Sep. 2016, pp. 1–5.
- [7] M. J. Pan and C. Randall, "A brief introduction to ceramic capacitors," *IEEE Electr. Insul. Mag.*, vol. 26, no. 3, pp. 44–50, May/June 2010.
- [8] A. Sheikholeslami and P. G. Gulak, "A survey of behavioral modeling of ferroelectric capacitors," *IEEE Trans. Ultrason., Ferroelectr., Freq. Control*, vol. 44, no. 4, pp. 917–924, Jul. 1997.
- [9] I. Novak, K. B. Williams, R. Miller Jason, G. Blando, and N. Shannon, "DC and AC bias dependence of capacitors," in *Proc. DesignCon*, Jan. 2011, pp. 1–16.
- [10] F. Maislinger, H. Ertl, G. Stojcic, C. Lagler, and F. Holzner, "Design of a 100 kHz wide bandgap inverter for motor applications with active damped sine wave filter," *The J. Eng.*, vol. 2019, no. 17, pp. 3766–3771, Apr. 2019.
- [11] J. W. Kolar, H. Ertl, and F. C. Zach, "Influence of the modulation method on the conduction and switching losses of a PWM converter system," *IEEE Trans. Ind. Appl.*, vol. 27, no. 6, pp. 1063–1075, Nov. 1991.
- [12] K. Taniguchi, Y. Ogino, and H. Irie, "PWM technique for power MOS-FET inverter," *IEEE Trans. Power Electron.*, vol. 3, no. 3, pp. 328–334, Jul. 1988.
- [13] M. Antivachis, D. Bortis, L. Schrittwieser, and J. W. Kolar, "Novel buck-boost inverter topology for fuel-cell powered drive systems," in *Proc. IEEE Appl. Power Electron. Conf. Expo.*, Mar. 2018, pp. 1492–1499.
- [14] D. Neumayr, D. Bortis, J. W. Kolar, M. Koini, and J. Konrad, "Comprehensive large-signal performance analysis of ceramic capacitors for power pulsation buffers," in *Proc. 17th IEEE Workshop Control Model. Power Electron.*, Jun. 2016, pp. 1–8.
- [15] S. Coday, C. B. Barth, and R. C. N. Pilawa-Podgurski, "Characterization and modeling of ceramic capacitor losses under large signal operating conditions," in *Proc. 19th IEEE Workshop Control Model. Power Electron.*, Jun. 2018, pp. 1–8.
- [16] L. E. Mosley, "Capacitor impedance needs for future microprocessors," in *Proc. 26th Symp. Passive Compon.*, Apr. 2006, pp. 193–203.
- [17] C. P. Steinmetz, "On the law of hysteresis," *Trans. Am. Inst. Electr. Eng.*, vol. IX, no. 1, pp. 1–64, Jan. 1892.
- [18] K. Venkatachalam, C. R. Sullivan, T. Abdallah, and H. Tacca, "Accurate prediction of ferrite core loss with nonsinusoidal waveforms using only Steinmetz parameters," in *Proc. IEEE Workshop Comput. Power Electron.*, Jun. 2002, pp. 36–41.
- [19] J. B. Goodenough, "Summary of losses in magnetic materials," *IEEE Trans. Magn.*, vol. 38, no. 5, pp. 3398–3408, Dec. 2002.
- [20] S. Ben-Yaakov, "Characterization of ferroelectric ceramic capacitors," in *Proc. 20th IEEE Eur. Conf. Power Electron. Appl.*, Sep. 2018, pp. 1–8.
- [21] "Equivalent series resistance (ESR) of capacitors," Tech. Rep. 035002 A4, QuadTech, Northumberland, U.K., 2007.
- [22] J. F. Scott, "Ferroelectrics go bananas," *J. Phys.: Condens. Matter*, vol. 20, no. 2, pp. 021001–021002, Dec. 2007.
- [23] G. Liu, S. Zhang, W. Jiang, and W. Cao, "Losses in ferroelectric materials," *Mater. Sci. Eng. R: Rep.*, vol. 89, pp. 1–48, Mar. 2015.
- [24] S. Ben-Yaakov, "Some observations on loss and hysteresis of ferroelectric-based ceramic capacitors," *IEEE Trans. Power Electron.*, vol. 33, no. 11, pp. 9127–9129, Nov. 2018.
- [25] J. B. Fedison and M. J. Harrison, " C_{oss} hysteresis in advanced super-junction MOSFETs," in *Proc. IEEE Appl. Power Electron. Conf. Expo.*, May 2016, pp. 247–252.
- [26] G. Zulauf, S. Park, W. Liang, K. N. Surakitbovorn, and J. Rivas-Davila, " C_{oss} losses in 600 V GaN power semiconductors in soft-switched, high- and very-high-frequency power converters," *IEEE Trans. Power Electron.*, vol. 33, no. 12, pp. 10748–10763, Jan. 2018.
- [27] C. P. Steinmetz, *Lectures on Electrical Engineering* Dover Phoenix Editions, vol. 3. New York, NY, USA: Dover, 2003.
- [28] C. B. Sawyer and C. H. Tower, "Rochelle salt as a dielectric," *Phys. Rev.*, vol. 35, pp. 269–273, Feb. 1930.
- [29] L. E. Mosley and J. S. Schrader, "Hysteresis measurements of multi-layer ceramic capacitors using a Sawyer-Tower circuit," in *Proc. 26th Symp. Passive Compon.*, Jan. 2007, pp. 285–295.
- [30] G. Zulauf, Z. Tong, J. D. Plummer, and J. M. Rivas-Davila, "Active power device selection in high- and very-high-frequency power converters," *IEEE Trans. Power Electron.*, vol. 34, no. 7, pp. 6818–6833, Oct. 2018.
- [31] M. S. Nikoo, A. Jafari, N. Perera, and E. Matioli, "Measurement of large-signal C_{oss} and C_{oss} losses of transistors based on nonlinear resonance," *IEEE Trans. Power Electron.*, vol. 35, no. 3, pp. 2242–2246, Sep. 2019.
- [32] J. M. Miller, C. W. Ayers, L. E. Seiber, and D. B. Smith, "Calorimeter evaluation of inverter grade metalized film capacitor ESR," in *Proc. IEEE Energy Convers. Congr. Expo.*, Sep. 2012, pp. 2157–2163.
- [33] H. H. Race and S. C. Leonard, "Calorimetric measurement of dielectric losses in solids," *Electr. Eng.*, vol. 55, no. 12, pp. 1347–1356, Dec. 1936.
- [34] A. Brockmeyer, "Experimental evaluation of the influence of DC-premagnetization on the properties of power electronic ferrites," in *Proc. IEEE Appl. Power Electron. Conf.*, Mar. 1996, vol. 1, pp. 454–460.
- [35] J. Muhlethaler, J. Biela, J. W. Kolar, and A. Ecklebe, "Core losses under the DC bias condition based on Steinmetz parameters," *IEEE Trans. Power Electron.*, vol. 27, no. 2, pp. 953–963, Feb. 2012.
- [36] M. Guacci *et al.*, "Experimental characterization of silicon and gallium nitride 200 V power semiconductors for modular/multi-level converters using advanced measurement techniques," *IEEE J. Emerg. Sel. Topics Power Electron.*, Sep. 2019.

- [37] S. Coday and R. C. N. Pilawa-Podgurski, "High accuracy calorimetric measurements and modeling of ceramic capacitor losses under large ripple operation," in *Proc. IEEE Appl. Power Electron. Conf.*, Mar. 2020, pp. 188–194.
- [38] R. M. Burkart, H. Uemura, and J. W. Kolar, "Optimal inductor design for 3-phase voltage-source PWM converters considering different magnetic materials and a wide switching frequency range," in *Proc. Int. Power Electron. Conf.*, May 2014, pp. 891–898.
- [39] W. G. Hurley and W. H. Wölfle, *Transformers and Inductors for Power Electronics: Theory, Design and Applications*. Hoboken, NJ, USA: Wiley, 2013.
- [40] J. T. Evans, "Characterizing ferroelectric materials," in *Proc. 19th IEEE Int. Symp. Appl. Ferroelect.*, Feb. 2010, pp. 1–123.
- [41] L. Hoffmann, C. Gautier, S. Lefebvre, and F. Costa, "Optimization of the driver of GaN power transistors through measurement of their thermal behavior," *IEEE Trans. Power Electron.*, vol. 29, no. 5, pp. 2359–2366, May 2014.
- [42] D. Rothmund, D. Bortis, and J. W. Kolar, "Accurate transient calorimetric measurement of soft-switching losses of 10 kV SiC MOSFETs and diodes," *IEEE Trans. Power Electron.*, vol. 33, no. 6, pp. 5240–5250, Jun. 2018.
- [43] P. Papamanolis, T. Guillod, F. Krismer, and J. W. Kolar, "Transient calorimetric measurement of ferrite core losses," in *Proc. 35th Appl. Power Electron. Conf. Expo.*, Mar. 2020, pp. 195–201.



David Menzi (Student Member, IEEE) received the B.Sc. and M.Sc. degrees in electrical engineering and information technology from the Swiss Federal Institute of Technology (ETH), Zurich, Switzerland, in 2015 and 2017, respectively. He is currently working toward the Ph.D. degree with the Power Electronic Systems Laboratory, Zurich.

He focused on power electronics, control theory, as well as high voltage technology and also spent a semester at the Royal Institute of Technology, Stockholm, Sweden, as an Exchange Student. During his studies, he worked at ABB Medium Voltage Drives, Turgi, Switzerland, as an Intern and a Working Student. His current research focuses on ultracompact three-phase inverter and rectifier systems with wide input/output voltage range.



Dominik Bortis (Member, IEEE) received the M.Sc. and Ph.D. degrees in electrical engineering from the Swiss Federal Institute of Technology (ETH), Zurich, Switzerland, in 2005 and 2008, respectively, and the Ph.D. degree from the Power Electronic Systems Laboratory (PES), ETH Zurich.

From 2008 to 2011, he was a Postdoctoral Fellow and from 2011 to 2016, a Research Associate with PES, co-supervising Ph.D. students and leading industry research projects. Since January 2016, he has been heading the research group, Advanced Mechatronic Systems, PES, which concentrates on ultrahigh speed motors, magnetic bearings and bearingless drives, new linear-rotary actuator, and machine concepts with integrated power electronics. His targeted applications include, e.g., highly dynamic and precise positioning systems, medical and pharmaceutical systems, and future mobility concepts. He has published 90+ scientific papers in international journals and conference proceedings and filed 30+ patents.

Dr. Bortis has received seven IEEE Conference Prize Paper Awards.



Grayson Zulauf (Student Member, IEEE) received the B.A. degree in engineering sciences and the B.E. degree in electrical engineering (with highest honors) from the Thayer School of Engineering, Dartmouth College, Hanover, NH, USA, in 2012 and 2013, respectively, and the M.S. degree in electrical engineering from Stanford University, Stanford, CA, USA, in 2019. He is currently working toward the Ph.D. degree in electrical engineering with the Stanford University Power Electronics Research Lab, Stanford University, Stanford, CA, USA.

From 2013 to 2016, he was an Electrical Engineer and Product Manager with Motiv Power Systems. In 2019, he was a ThinkSwiss Research Fellow with the Power Electronics System Laboratory, Federal Institute of Technology, Zurich, Switzerland. His research focuses on extending high- and very-high-frequency resonant converters to electrified transportation applications.

Dr. Zulauf is a Stanford Graduate Fellow and a National Science Foundation Graduate Research Fellow.



Morris Heller (Student Member, IEEE) received the B.Sc. degree in electric engineering from Hochschule Luzern/FHZ, Luzern, Switzerland, in 2014, and the M.Sc. degree in electrical engineering and information technology, with a focus on power electronic systems design and power semiconductors technology, in 2018, from the Swiss Federal Institute of Technology (ETH), Zurich, Switzerland, where he is currently working toward the Ph.D. degree with the Power Electronic Systems Laboratory.

His research focuses on three-phase rectifiers and multiport power converters.



Johann W. Kolar (Fellow, IEEE) received the M.Sc. and Ph.D. degree (*summa cum laude/promotio sub auspiciis praesidentis rei publicae*) from the Vienna University of Technology, Vienna, Austria, in 1997 and 1999, respectively.

Since 1984, he has been working as an independent Researcher and international Consultant in close collaboration with the Vienna University of Technology, in the fields of power electronics, industrial electronics, and high-performance drive systems. He is currently a Full Professor and the Head of the Power

Electronic Systems Laboratory, Swiss Federal Institute of Technology (ETH), Zurich, Switzerland. He has proposed numerous novel PWM converter topologies, modulation and control concepts, multiobjective power electronics design procedures, etc., and has supervised 70+ Ph.D. students. He has published 900+ scientific papers in international journals and conference proceedings, four book chapters, and has filed 190+ patents. He has presented 30+ educational seminars at leading international conferences, and served as IEEE PELS Distinguished Lecturer, from 2012 to 2016. His current research interests include ultracompact and ultraefficient SiC and GaN converter systems, ANN-based power electronics components and systems design, solid-state transformers, power supplies on chip, as well as ultrahigh speed and ultralight weight drives, bearingless motors, and energy harvesting.

Dr. Kolar has received 34 IEEE Transactions and Conference Prize Paper Awards, the 2014 IEEE Power Electronics Society R. David Middlebrook Achievement Award, the 2016 IEEE William E. Newell Power Electronics Award, the 2016 IEEE PEMC Council Award, and two ETH Zurich Golden Owl Awards for excellence in teaching. He has initiated and/or is the Founder of four ETH spin-off companies.